# Analysis of the Afterpulsing and the Dark Noise Spectrum From the DEAP-3600 Detector

by

Kamal Singhrao

A thesis submitted in partial fulfillment of the requirements for the degree of

Master of Science

Department of Physics
**University of Alberta**

# Abstract

The DEAP-3600 experiment is a 3600 kg Liquid Argon (LAr) target scintillation detector designed to detect the Weakly Interacting Massive Particle (WIMP) dark matter candidate. The detector works by detecting photons released by nuclear recoils of Argon nuclei, using an array of 255 nearly isotropically placed photomultiplier tubes (PMTs). The detector electronics system then digitizes the pulse detected by the PMTs and is designed to maximize discrimination between single and multiple photon pulses. The data processing chain is completed with an offline processor that discriminates the dominant Ar-39 induced $\beta$ decay background from nuclear recoil induced hits using pulse shaped discrimination (PSD).

Each PMT has an intrinsic level of background caused by dark noise and afterpulsing that can potentially create anomalous signals in the WIMP region of interest. Dark noise is caused by photoelectrons being spontaneously emitted from the PMT photocathode material and afterpulsing is typically caused by the residual gas ions inside the PMT that drift and strike the photocathode resulting in the emission of many photoelectrons. This thesis introduces a method to characterize the levels of PMT afterpulsing and dark noise in the DEAP-3600 detector. Presented is a discussion of the implications of the resultant PMT background for the WIMP search during the detector physics data running.

# Preface

The work presented in this thesis is the author's own and is original except where noted here. The use of others' work is cited in the text where appropriate.

The DEAP-3600 detector is the result of an international collaboration of scientists, developed over a period of nearly 8 years. Given this, it is natural in such projects to participate in a number of collaborative efforts and build on the work of others' while completing a graduate degree. Within this thesis, the single photoelectron gain plots (included in Chapter 4) were produced by collaborators Thomas Li and Tina Pollmann (SNOLAB). The code that generates the charge versus $\Delta$t histograms and related 1D projections (Chapter 4) where developed as a joint effort by the author and co-supervisor Fabrice Retiere (TRIUMF). The fitting function, both the original algorithm and software, was developed initially by co-supervisor Retiere and subsequently modified by the author to produce the results presented in the thesis. The raw PMT waveform plots presented in the Chapter 4, that make it possible to determine if the charge versus $\Delta$t hits were from a real physics event, were produced Benjamin Smith (TRIUMF) using the DEAP-3600 online data display tool. The photomultiplier tube uniformity study plots (Chapter 5) were produced by the author using the resultant data from code generated by co-supervisor Retiere. Finally, the Fprompt analysis code utilized for the results in Chapter 6 was produced originally by co-supervisor Retiere and modified by the author for the purpose of the thesis studies.

# Acknowledgements

I would like to take this opportunity to thank several groups of people who help me over these two long years. Firstly, I would like to express thanks to my advisors Fabrice Retiere and Darren Grant in addition to my thesis committee Aksel Hallin and Gregory Sivakoff. I also want to express thanks to folks on the DEAP collaboration who were influential to me as scientists namely Pierre Gorel, Chris Jillings and Benjamin Smith. Additionally, I would like to express my admiration to Tony Flower and all those responsible for the DEAP-3600 experiment construction.

Outside of the experiment, there were a variety of people and groups who helped maintain my sanity. Namely the Vancouver Rock Climbing group, the Alpine Club of Canada and notably Lennart Huth whose persistence lead me to learn how to ski and increase my drinking tolerance to almost Germanic levels! Additionally, I would like to thank Anne-Marie Comte whose 6am climbing sessions made me a stronger person mentally and physically. Additionally, I would like to say to thanks to Erin Bailey, Christopher Hollingshead and Skyler Freeman and Thomas McElroy who helped make my summer at SNOLAB awesome.

Finally, I want to thank my Parents and Siblings for all their support while I was jetting around Canada.

# Contents

# List of Figures

# List of Tables

# List of Abbreviations

2dFGRS 2 degree Field Galaxy Redshift Survey

AARF Aluminum and Acrylic Reflector and Fiber

AMS Alpha Magnetic Spectrometer

ASUM Analog Sum

AV Acrylic Vessel

CDM Cold Dark Matter

CDMS Cryogenic Dark Matter Search

CMB Cosmic Microwave Background

DAQ Data Acquisition

DEAP-3600 Dark Matter Experiment using Argon Pulse Shaped Discrimination

DSPE Derivative Single Photoelectron

DTM DEAP Trigger Module

EROS Exprience pour la Recherche d'Objets Sombres

Fermi-LAT Fermi-Large Area Telescope

LSP Lightest Supersymmetric Particle

LUX Large Underground Xenon

LZ Lux-Zeplin

MACHO Massive Compact Halo Object

MSSM Minimum Supersymmetric Standard Model

PAMELA Payload for Anti-Matter Exploration and Light-nuclei Astrophysics

PC Personal Computer

PMT Photo-Multiplier Tube

RAT Reactor Acquisition Tool

SCB Signal Conditioning Board

SD Spin Dependent

SDSS Sloan Digital Sky Survey

SI Spin Independent

SPE Single Photoelectron

Super-K Super-Kamiokande

SUSY Supersymmetry

WArP WIMP Argon Programme

WIMP Weakly Interacting Massive Particle

# Chapter 1

# Introduction

One of the primary challenges in science for nearly 80 years has been the search for an explanation to the Dark Matter component of the Universe [1]. Recent developments in astrophysical measurements [2] have provided refined precision on our knowledge of a Universe with a Dark Matter dominated matter energy density. With no viable astrophysical explanation for this observation, the effort to provide a particle physics explanation to resolve this mystery has continued to grow [3]. In particular, the past decade has witnessed a large build-up experimental searches for a Dark Matter particle candidate, the favorite being the Weakly Interacting Massive Particle (WIMP) [4].

The DEAP-3600 experiment [5] is a large scintillation experiment designed to detect WIMP-induced nuclear recoils inside a 3,600 kg target volume of liquid Argon contained inside an acrylic vessel. The experiment is located nearly 2 km below the Earth's surface in the Vale Creighton Mine near Sudbury, Ontario, Canada and is designed to provide world-leading sensitivity to the WIMP-nucleon spin independent cross-section for WIMP masses above approximately 60 GeV. The scintillation light produced in the candidate signal events in DEAP-3600 is ultimately detected by photomultiplier tubes (PMTs) that provide nearly 72% isotropic coverage of the vessel [5]. The data from the events are then generated using the amplified signal from the PMTs and output via a system of sensitive electronics that, with an online analysis algorithm, determine the type of event that occurred in the detector.

This thesis presents a detailed study of two of the primary inherent sources of operating backgrounds associated with utilizing PMTs in these type of Dark Matter search detectors; namely dark noise and afterpulsing. The full characterization of these PMT backgrounds is crucial to understanding the DEAP-3600 detector response and, therefore, ultimately impacts the achievable sensitivity to the WIMP signal. In Chapter 2 the reader will find the historical motivation for Dark Matter being prevalent in the Universe and a discussion of the current complementary searches that have been developed for WIMP candidate Dark Matter: direct, indirect and production at high energy colliders. Chapter 3 provides the reader with a detailed description of the DEAP-3600 detector including the motivation for its design elements. Chapter 4 discusses the potential sources and mechanisms of dark noise and afterpulsing as PMT backgrounds. Additionally, we present in Chapter 4 a method to extract the necessary parameters to describe dark noise and afterpulsing using a novel fitting algorithm applied to the late PMT waveform for initial single photoelectron-like pulses. Chapter 4 concludes with a comparison test of the late pulse spectrum from externally produced photoelectrons from a laser source to the spectrum from the DEAP-3600 detector when operated in a dark state. In Chapter 5 the reader will find the global studies that test the uniformity of the complete suite of DEAP-3600 PMTs for the dark noise and afterpulsing backgrounds. Also presented is the response of the PMTs to variations in the operating voltage and how this may affect the late pulse fit parameters. The thesis concludes with Chapter 6, where the reader will find a discussion of the implications for the measured levels of PMT afterpulsing in DEAP-3600 on the soon to begin WIMP search data runs and possible methods to mitigate their impact.

# Chapter 2

# The WIMP hypothesis

## 2.1 Introduction

Over the past century there has been an enormous effort to try to understand the nature and origin of Dark (non-luminous and non-absorbing) Matter. Dark Matter is proposed explanation for a number of astrophysics challenges, including why certain galaxies appear to be rotating faster than predicted by Newtonian gravity if they were only comprised of luminous (baryonic) matter [6]. Here we will introduce the evidence that supports the existence of Cold Dark Matter (CDM), a proposed solution to the Dark Matter problem [7] [8] [9]. We will discuss the favoured Dark Matter candidate, the Weakly Interacting Massive Particle (WIMP), and how WIMPs may be supersymmetric (SUSY) particles [10]. We present the types of interactions we might see from SUSY WIMP candidates and how we might be able to detect them with a detector like DEAP-3600. We will close with a discussion on the current status of WIMP searches.

## 2.2 Observational Evidence

### 2.2.1 Galactic Rotation Curves

The first evidence for dark matter was proposed by Fritz Zwicky, whose application of the Virial theorem on the rotational velocities of the galaxies in the Coma cluster led to a much larger cluster mass than predicted by Newtonian gravity [1]. Further evidence from studies of galactic rotation curves strengthened his hypothesis [6]. From Newtonian dynamics the rotation velocity $v(r)$ of the galaxies is expected to fall off as

$$v(r) = \sqrt{\frac{GM(r)}{r}}, \tag{2.1}$$

where G is the Gravitational constant, M(r) is the galaxy mass as a function of the distance from the source, $r$. If the mass density profile of the galaxy is like an optical disk (where the surface brightness declines exponentially with radius) the galactic masses should be approximately independent of $r$ if they are treated as a point source mass, meaning that the galactic velocity falls off as approximately $v(r) \propto 1/\sqrt{(}r)$. However, as demonstrated by Fig. 2.1 the rotation curves of galaxies are flat at large radii resulting in the need for a halo with $M(r) \propto r$ at large radii and a galactic density $\rho(r) \propto 1/r^2$ [11]. The dark matter density is typically described in terms of its density parameter, $\Omega_{\mathrm{DM}} = \rho/\rho_{\mathrm{critical}}$ where $\rho_{\mathrm{critical}}$ is the critical density that if smaller would cause the Universe to expand forever. The total density parameter of the Universe $\Omega$ is the sum of the dark matter component, $\Omega_{\mathrm{DM}}$, the baryonic matter component $\Omega_{\mathrm{M}}$ and the mass density of relativistic particles $\Omega_{\mathrm{rel}}$ [12]. Absence of sufficient luminous matter in the galaxies at large radii indicate the need for a dark matter component with a lower bound in the density to be $\Omega_{\mathrm{DM}} \geq 0.1$ [13] [14] [15].

### 2.2.2 Gravitational Lensing and Galactic Events

Gravitational lensing surveys have provided good estimates of how much dark matter is in individual galaxy clusters. The strong lensing method uses the concept of the Einstein ring,

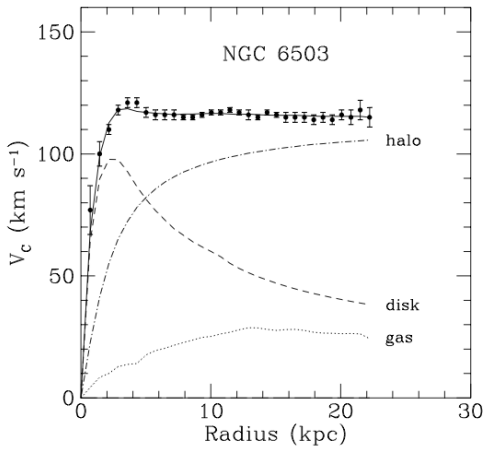


Figure 2.1: Rotation curve for the dwarf spiral galaxy NGC 6503 and the expected velocity contributions from the dark matter halo, optical disk and residual gas. Subtracting off the disk and gas contributions from the observed profile results in a velocity dispersion reminiscent of a galactic halo [16].

which is a distortion of space-time by a large interstellar objects [17]. This affects the path of light from a distant source such as a star or a galaxy enabling the massive object to act as a lens when they obstruct the line of sight between an observer and the source [18].

This method has aided the dark matter search in two primary ways. First, gravitational microlensing has helped discount the Massive Compact Halo Object (MACHO) hypothesis. MACHOs are interstellar objects that are made entirely of baryonic matter [19]. The search for MACHOs used the microlensing effect, which relies on the MACHO to pass in front of a star to make it appear brighter than it actually is [20]. Based on microlensing observations by the EROS2 collaboration, MACHOs in the mass range of $0.6 \times 10^{-7} M_{\odot} < M < 15 M_{\odot}$ were ruled out as the primary occupants of the Milky Way halo [21] . This naturally led the dark matter community to turn their attention to the WIMP as being the primary dark matter candidate [22].

Second is the observation of astrophysical events such as the Bullet Cluster as shown in Fig. 2.2. This event resulted from the collision of two galaxy clusters approximately 150 million years ago where the concentrations of hot gas from the clusters collided, passed

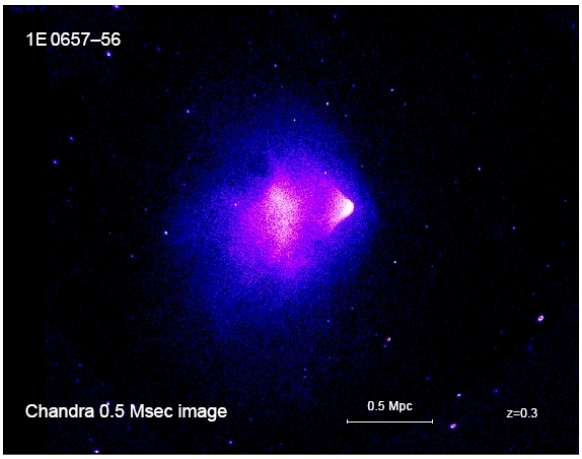


Figure 2.2: X-ray observation of the Bullet Cluster by the Chandra X-ray observatory. There are two distinct parts of the nucleus representing the collision point of the two galactic clusters. The gases dominate the visible mass budget of the clusters. The purple regions represents the stellar and gaseous matter and the purple region represents the dark matter region. The dark matter distribution was resolved using weak lensing. [23].

through each other and stopped close to the point of impact [24]. Measurements of the mass density via lensing demonstrated that most of the mass after the collision was located away from the hot gas cluster. With a statistical significance of $8\sigma$, this allowed for limits to be placed on the self interaction cross section of dark matter and gave experimental evidence that the dark matter self-interactions were indeed weak [24].

### 2.2.3 CMB Distribution

Galactic rotation curves provide us with compelling evidence that there might be dark matter. The total amount of dark matter in the Universe can be understood by analyzing the Cosmic Microwave Background (CMB) spectrum. The CMB spectrum is a blackbody spectrum with a temperature of 2.725K comprised of relic photons from soon after the Big Bang [25]. The most sensitive measurement of the CMB comes from the Planck telescope [26]. Planck measured the temperature fluctuations of the CMB, which enabled small and large scale anisotropies in the sky to be well characterized. The CMB anisotropies enable accurate testing of cosmological parameters. The main conclusion from analysis of the Planck data is the abundance of baryonic matter $\Omega_{\mathrm{b}}$ from the fits to the multipole expansion as shown

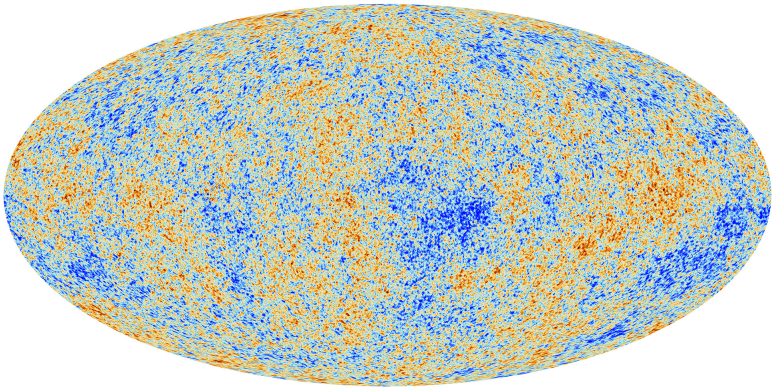

Figure 2.3: The all sky picture of the temperature in the early universe taken by the Planck telescope. The color-scale represents CMB temperature fluctuations and correspond to seeds for galaxy formations [2].

in Fig. 2.4, is insufficient to account for the physical matter density $\Omega_{\mathrm{M}}$. Quantitatively, the abundances found by Planck were,

$$\begin{aligned} \Omega_b h^2 &= 0.02226 \pm 0.00023 \\ \Omega_M h^2 &= 0.1415 \pm 0.0019 \end{aligned} \tag{2.2}$$

meaning that baryonic matter accounts for 17% of the total matter density [2]. It is clear from these results that the abundance of baryonic matter in the Universe is not sufficient to account for the total physical matter [27]

## 2.3 Expected WIMP Distributions and Behaviors

### 2.3.1 WIMPs in the Early Universe

Simulations of the dark matter distribution in the Galaxy imply that dark matter is non relativistic (cold). The WIMP properties fit well with this prediction and with the relic particle model from the early Universe when all particles were assumed to be in a state of thermal equilibrium production [11]. When the temperature of the Universe dropped below that required to thermally produce WIMPs, the WIMP number density decreased

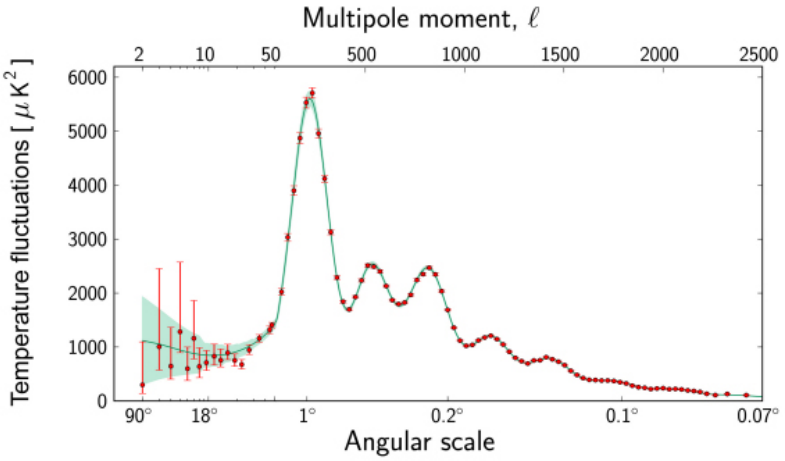


Figure 2.4: Shown is the temperature flucutations measured by Planck as a function of angular scale. The red points show the measured CMB temperature fluctuations as a function of angular scale on the sky as seen by Planck. The green shaded region shows the expected temperature fluctuations by the best fit of the standard model of the Universe and the fit of the Planck data points is also shown. The relative sizes of the first three peaks gives a very precise idea of how much baryonic and dark matter there is in the Universe [2].

exponentially and the annihilation rate $\tau = \langle \sigma\nu \rangle \, n_\chi$ fell. As a result of this drop in rate, WIMPs fell out of equilibrium leaving a relic abundance [13].

The current cosmological WIMP abundance $\Omega_\chi$ can be determined by solving the Boltzmann equation, which yields an approximate solution of

$$\Omega_\chi h^2 = \frac{m_\chi n_\chi}{\rho_c} \simeq \left( \frac{3 \times 10^{-27} \text{ cm}^3 \text{ sec}^{-1}}{\sigma \text{ v}} \right) \tag{2.3}$$

where $m_\chi$ is the WIMP mass, $\rho_c$ is the critical WIMP density, $h$ is the Hubble constant in units of 100 km sec$^{-1}$ Mpc$^{-1}$ and $\sigma_A v$ is the WIMP cross section. To get the same cosmological abundance for dark matter, the WIMP annihilation cross section is approximately $10^{-9}$ GeV$^{-2}$ [11]. Additionally, this cross section would also be expected from a typical electroweak cross section $\sigma_{\text{weak}} \simeq \alpha^2 / m^2_{\text{weak}}$ for a (low mass) 100 GeV WIMP [14]. This link between electroweak physics and early big bang physics is a coincidence that is commonly referred to as the WIMP miracle [28].

### 2.3.2 Large Scale Structure

Dark matter distributions have been reconstructed from sky surveys such as the 2 degree Field Galaxy Redshift Survey (2dFGRS) and the Sloan Digital Sky Survey (SDSS) and other observations such as high quality sky images. An example reconstruction is shown in Fig. 2.5. These surveys and the CMB spectrum measured by the Planck satellite provide evidence that enables the formation of galactic components to be tracked from 380,000 years after the Big Bang to the present day.

To track the evolution of structures from seed inhomogeneities such as primordial density fluctuations, N body simulations are used. N body simulations numerically calculate the growth of density perturbations. This is done by evolving the trajectories of a very large number of particles for an expanding Universe. The expansion is modeled by solving a dynamical equation such as Poisson's equation [29] . The main findings of these simulations were that dark matter is necessary to explain structure formation. Observations have suggested that structure formation proceeds hierarchically with the smaller structures collapsing first, followed by galaxies, and then followed by clusters of galaxies. Dark matter is required to compact structure during this evolution. The second major finding from N-body simulations is that dark matter has to be cold for the structure formation model to succeed. Additionally, the cold dark matter (CDM) model produces simulations that are consistent with the observations by the SDSS and 2dFGRS surveys [30] [31].

### 2.3.3 Summary

Based on the evidence presented, a viable dark matter candidate must have a number of distinct characteristics. To be a seed for large-scale structure formation the candidate has to be cold and must be dark. For the candidate to be a Big Bang relic and detectable it must have a lifetime longer than the age of the Universe. Finally, from the Bullet Cluster observation the candidate has to be weakly interacting.

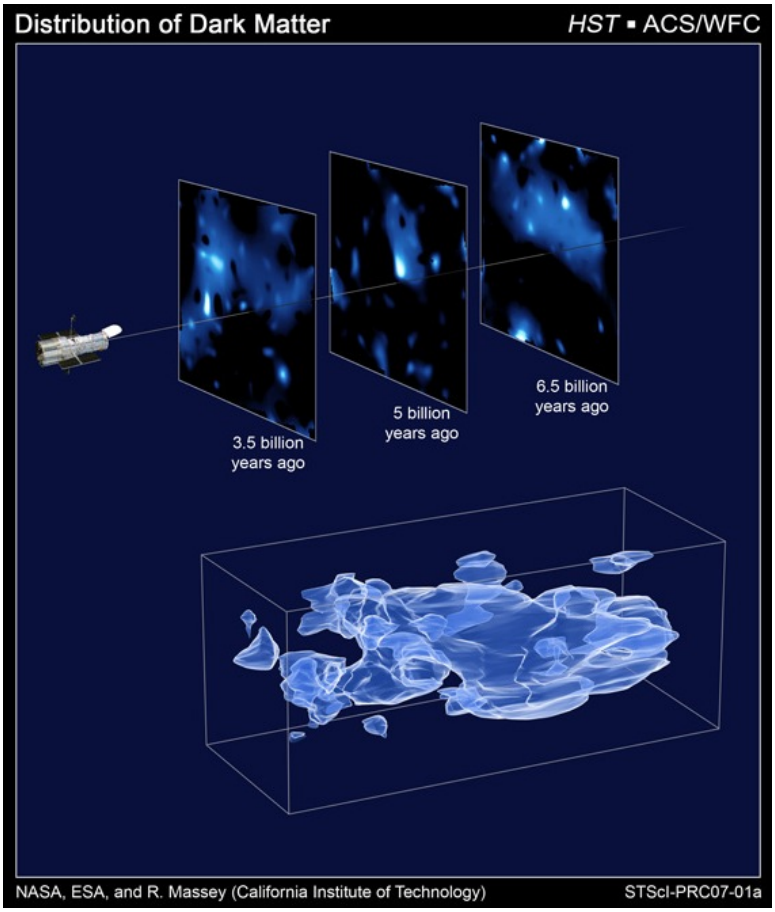


Figure 2.5: 3D distribution of Dark Matter in our local Universe constructed from the Hubble Map data. Each of the dark matter distributions at the three different times were created using snapshots of the CMB for galaxies at different times. It is calibrated by measuring the cosmological redshift of the lensing galaxies used to map the dark matter distribution. The slices across the Universe are combined to produce a 3D map of the dark matter distribution [32].

## 2.4 Supersymmetric Dark Matter

### 2.4.1 Overview

A theoretical model that is widely used to describe the WIMP is that provided by supersymmetry. Supersymmetry is an extension of the Standard Model and was constructed to explore new physics that might arise between the electroweak ($\approx 10^2$ GeV) and the Planck scale ($\approx 10^{19}$ GeV) [33]. Since the WIMP is expected to have a mass within this range, it

is only natural to explore the possibility that the WIMP may be supersymmetric in nature. To maintain simplicity, here we discuss supersymmetry in terms of the Minimum Supersymmetric Model (MSSM) and do not divert into the general supersymmetric model or other topics such as supergravity.

### 2.4.2 The Hierarchy Problem

A major piece of the Standard Model is the existence of a Higgs field and consequently a Higgs boson [33]. Spontaneous symmetry breaking of the Higgs field explains why gauge bosons have mass. However, there is a problem with the current form of the Standard Model where the Higgs can couple with virtual fermions. Adding these virtual fermion loops continually to the Higgs interactions means that there are extra terms in the Higgs Lagrangian that results in the Higgs having a much lower mass than the Planck mass [34] [4]. This is known as the Hierarchy Problem. A solution to this problem is to define another symmetry where these virtual fermions are actually virtual scalar particles. This causes the virtual fermion contribution to the Higgs Lagrangian to cancel, thereby restoring the Higgs mass to a value much lower than the Plank mass. The existence of these virtual scalar particles, each with masses going up to the Plank scale, provides the basis for the supersymmetric model [4].

### 2.4.3 R Parity and Neutralinos

In order for supersymmetry to produce experimentally viable interactions the baryon number $B$ and lepton number $L$ of supersymmetric interactions, must be conserved [14]. This prevents unphysical decay channels, such as proton decay: $\mathrm{p} \rightarrow \mathrm{e}^{+}\pi^{0}$ [4]. To conserve these two quantities an extra symmetry called R parity, $P_R$, is introduced defined by

$$P_R = (-1)^{3(B-L)+2s}, \tag{2.4}$$

where $s$ is the spin. The phenomenological consequence from R parity conservation is that the lightest supersymmetric particle (LSP) must be stable. If the LSP is a weakly

interacting electrically neutral particle, then it is an excellent WIMP candidate. The lightest supersymmetric dark matter candidate, whose mass has not been disfavored by collider experiments, is the neutralino [4]. Since the WIMP candidate is expected to be slow moving, the most relevant neutralino interactions for detection are self annihilation and nucleon elastic scattering [13].

## 2.5 Current Status of WIMP Searches

WIMP searches are generally divided into three distinct complimentary fields: direct detection, indirect detection (detection of WIMP decay and annihilation products), and production at colliders. The direct and indirect experiments can also be subdivided into spin independent (SI) and spin dependent (SD) experiments. The SD experiments are sensitive to the spin state of WIMP-like nuclear recoils, whereas SI experiments are not [35]. SD experiments enable a specific interaction model to be identified if a WIMP is detected [35].

### 2.5.1 Direct WIMP Searches

Direct WIMP searches are reliant on measuring the energy imparted from a WIMP-nucleon interaction. There are three primary mechanisms of detecting the nuclear recoil energy: ionization, scintillation, and phonon production. Some experiments use more than one of these mechanisms. Ionization based experiments rely on measuring the ions produced as a result of a WIMP interacting with a target. Phonon based experiments involve the nuclear recoil produced from a WIMP interaction with a target solid producing a phonon. As a result a signal is measured from a temperature change if the detection medium is a crystal or from a phase transition if the detection medium is a superheated liquid. Scintillation experiments rely on the detection of scintillation light produced from the excited state of a WIMP-induced nuclear recoil, such as in DEAP-3600. Using these different methods, stringent limits on the WIMP-nucleon cross section and the WIMP mass can be placed, as demonstrated in Fig. 2.6. The lower cross section limit for WIMP detection also as demonstrated in Fig. 2.6, is determined by the irreducible neutrino backscattering events,

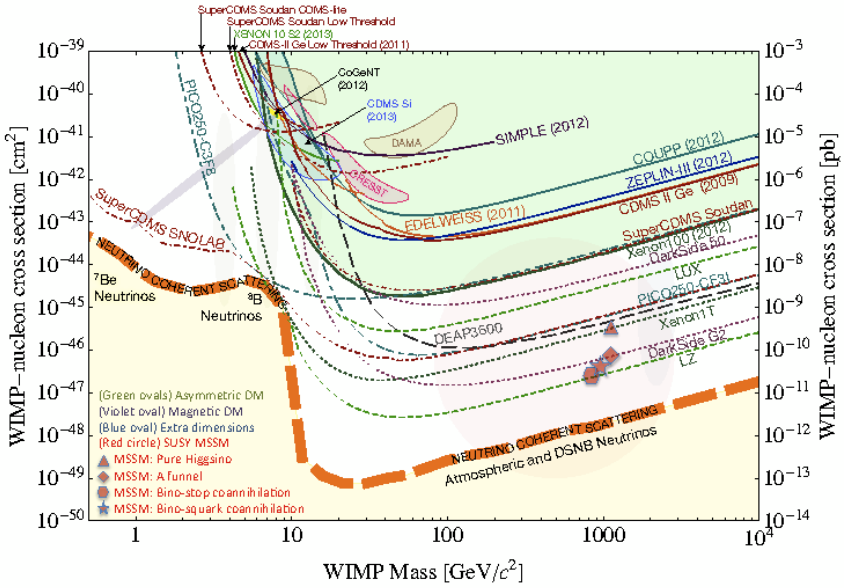


Figure 2.6: Spin Independent WIMP cross sections vs mass for a variety of experiments. The region colored in green is the parameter space that has been probed. The yellow region represents the atmospheric neutrino background scattering limit. Most of the current theories (that have not already been discounted) predict a 100 GeV WIMP candidate at a cross section between $10^{-45}$ cm$^{-2}$ to $10^{-47}$ cm$^{-2}$ [36].

the point where neutrinos start interacting with nucleons. Examples of experiments that utilize these detection techniques are discussed in the following section.

### Ionization and Phonon Based Detectors

Ionization and phonon based detectors such as CDMS (Cryogenic Dark Matter Search), measure ionization and phonon production from nuclear recoils, for example in semiconductor crystal substrates. The substrates are typically reverse biased to be sensitive to small voltage changes. Background discrimination for these types of detectors is based on the ratio of phonon to ionization signal. Experiments such as CDMS have their substrates held at mK temperatures, enabling high sensitivity to phonon induced temperature changes and event-by-event discrimination between electronic and nuclear recoil rates. Germanium and Silicon are used because they are semiconductors and can be made of high purity with low levels of intrinsic background radiation [37].

**Scintillation Detectors**

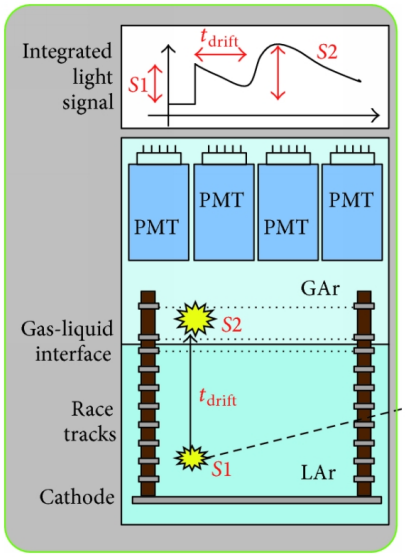


Figure 2.7: Schematic of the WARP dual phase dark matter experiment. The active fiducial volume is in the liquid phase of the experiment and the integrated light signal plot can be built from the signal propagated in the liquid and gas phases of the detector [38].

These detectors are designed to detect scintillation light from WIMP-induced nuclear recoils. The target volume can be a solid, such as Sodium Iodide for the DAMA/NaI experiment, a liquid noble gas, like Argon for the DEAP/CLEAN experiments or include a gas/dual phase such as in the WIMP Argon Programme (WArP) experiment or the Large Underground Xenon (LUX) experiment. The single and dual phase experiments use the total emitted light as a function of time as a discrimination parameter to distinguish between WIMP-like and gamma and electron induced events. A schematic of a dual phase setup is shown in Fig. 2.7, involving a set of Photo-Multiplier Tubes (PMTs) to detect light from the liquid phase and another set to detect light from the gaseous phase. This results in two light signals being produced from a single recoil. The amplitude of the light signal from the liquid phase of the experiment is known as S1 and the gaseous phase is known as S2. The parameters S1 and S2 can be weighted with different parameters. For example, LUX uses energy, position, recoil type, and electroluminescence (S2) to discriminate out background.

A WIMP like nuclear recoil in LUX would release a certain amount of scintillation light and be a single scatter event. Using position reconstruction and the ratio of S1/S2 a stringent discrimination parameter can be introduced to minimize background induced signals [39]. The single-phase DEAP-3600, the detector of interest for this work, is a scintillation detector and is discussed in detail in Chapter 2.

**Current Results**

Fig. 2.6 shows the major results of most current Spin Independent WIMP searches. The most sensitive limits on the WIMP mass have been achieved by the LUX experiments. At the time of writing, DEAP-3600 is currently in its early stages of calibration data acqusition and the WIMP search is expected to begin late 2015. There are a number of proposed experiments to probe as much of the WIMP parameter space as possible, including the SuperCDMS experiment at SNOLAB (sensitive to 1 GeV to 10 GeV WIMP masses) and the proposed Lux-Zeplin (LZ) and Darkside collaborations, aiming to push their sensitivities to within an order of magnitude from the neutrino backscattering limit.

### 2.5.2 Indirect WIMP Searches

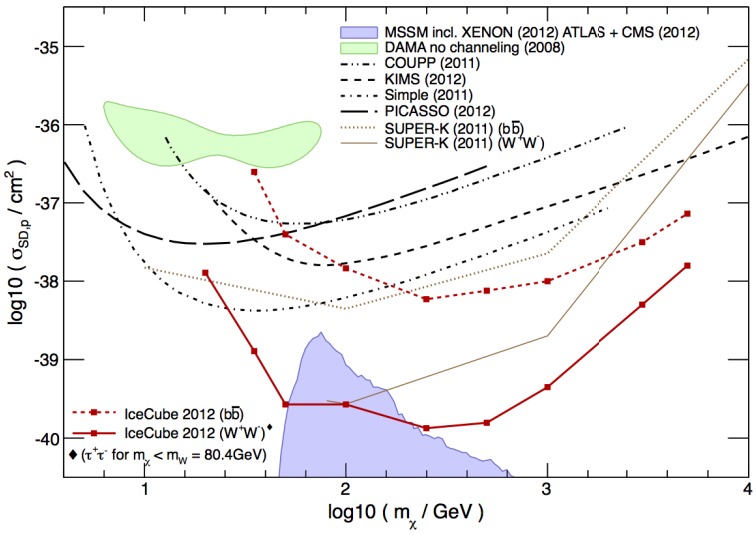


Figure 2.8: Spin dependent cross section for IceCube and SuperK with several direct searches shown for comparison. The indirect searches have the potential of complementing the direct searches and in the case of IceCube exceed the sensitivity of direct WIMP searches [40].

Indirect WIMP searches primarily involve trying to detect products of WIMP annihilations or decays. Regions of high matter density provide potential sources for large numbers of WIMP interactions. Examples of such targets are the Sun, galactic halos or dwarf galaxies [41]. Messenger particles, such as $\gamma$-rays or particle- antiparticle pairs, could be produced from these interactions. The messenger particles may then be detected and, based on their abundance, flux, and energy, fitted to models or provide WIMP mass - energy exclusion curves that are complimentary to the direct WIMP searches, as demonstrated in Fig. 2.8. Here, we discuss several experiments that could help draw conclusions about WIMPs and dark matter via indirect detection, including the Alpha Magnetic Spectrometer (AMS02) spectrometer (which is designed to measure the cosmic ray antiproton flux), the Fermi-LAT telescope (which is a pair conversion telescope), IceCube, and SuperK (water Cherenkov neutrino detectors).

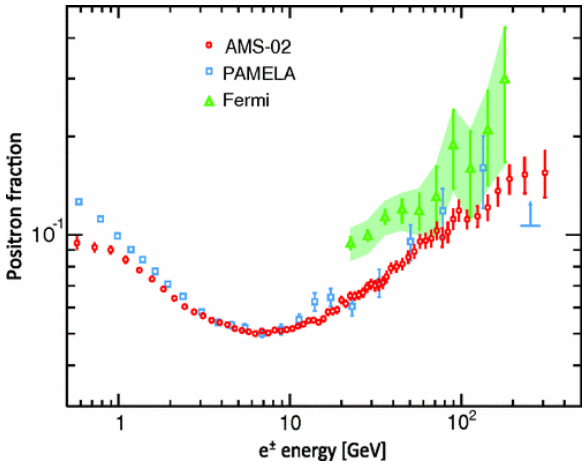


Figure 2.9: Positron fraction as a function of energy as measured by the PAMELA(blue), Fermi-LAT (Green) and AMS02 (red). It was expected that the positron fraction would decay exponentially; however there is a marked rise at energies of about 100GeV. This might be an indication of the presence on a new heavy particle at these energies or unknown physics [42].

The AMS02 experiment is a spectrometer installed on the International Space Station to measure the positron and electron flux in outer space [42]. The detector is made up of a series of smaller detector modules including a transition radiation detector, a ring imaging Cherenkov detector (to measure particle velocity), a time of flight counter, a silicon tracker (to measure particle coordinates), and a calorimeter (to measure the particle energy). Previous studies by the Payload for Anti-Matter Exploration and Light-nuclei Astrophysics (PAMELA) spectrometer (an earlier space based spectrometer that was designed to distinguish $e^{\pm}$ from $p/\bar{p}$ and He) implied an increase of the positron fraction at GeV energies, as shown in Fig. 2.9 [43]. The AMS02 was designed to improve on the large uncertainties of the PAMELA experiment. Their findings have demonstrated there is a marked increase in the positron fraction between 10 GeV to 200 GeV, possibly indicating some WIMP-like annihilation. Additionally, the energy range of the rise of the rise in positron fraction agrees well with the expected WIMP mass range from relic production [42].

The Fermi-LAT detects gamma rays that strike tungsten foils resulting in pair production [43]. The electron-positron pair are then detected by silicon micro strip detectors. Particle energy is measured using a scintillation crystal calorimeter and plastic scintillator tiles, with

wavelength shifting fibers being used as anti-coincidence detectors. The results of Fermi-Large Area Telescope (Fermi-LAT) are also compared in Fig. 2.9. For the energy sensitive region, the findings agree with the AMS and PAMELA experiments with an increase in positron fraction between 20 GeV to 300 GeV.

The IceCube experiment is an Earth-based neutrino telescope located at the South Pole in Antarctica [40]. The detector consists of 5160 Digital Optical Modules on 86 strings deployed over 1 cubic-km in the deep glacier. Each DOM contains a 10-inch Photo-Multiplier Tube (PMT) and a full data acquisitor. The PMTs are designed to detect Cherenkov light emitted by leptons produced by neutrinos interacting in the ice. If neutrinos are emitted from WIMP interactions in astrophysical bodies, the IceCube experiment has sensitivity to the cross section and energy of the WIMP particle. Two major results have been published from indirect WIMP searches by IceCube. The first was on the limits on the muon flux from neutralino annihilations in the Sun and the second was results from searches for Dark Matter annihilation in nearby galaxies and galaxy clusters [41]. IceCube did not see an excess of muon neutrinos over the atmospheric background. Additionally, they were able to put limits on the spin dependent WIMP-proton cross section as demonstrated in Fig. 2.8 for the $b\bar{b}$ and $W^+W^-$ channels for masses above 35 GeV. The search for neutrino excesses from the direction of the Virgo and Coma galaxy clusters as well as a variety of dwarf clusters yielded no significant excess in the neutrino count.

The Super Kamiokande (SuperK) has also set limits on the WIMP mass and interaction cross section. The SuperK experiment is a 50,000 ton water Cherenkov detector located in the Kamioka-Mozumi mine in Japan with 1,000 m of rock coverage [44]. It consists of an inner detector with 11,146 50 cm PMTs and an outer detector with 1,885 outward facing 20 cm PMTs. The indirect search conducted by SuperK put limits on the WIMP cross section and energy based on the muon neutrino flux from the direction of the Sun. A summary of their results is also shown in Fig. 2.8. Based on their analysis they were able to put stringent limits on WIMPs produced by the $b\bar{b}$ and $W^+W^-$ channels.

The Large Hadron Collider (LHC) is currently the premier location to detect WIMP production due to its high energy and lumonosity [10]. There have been a number of limits

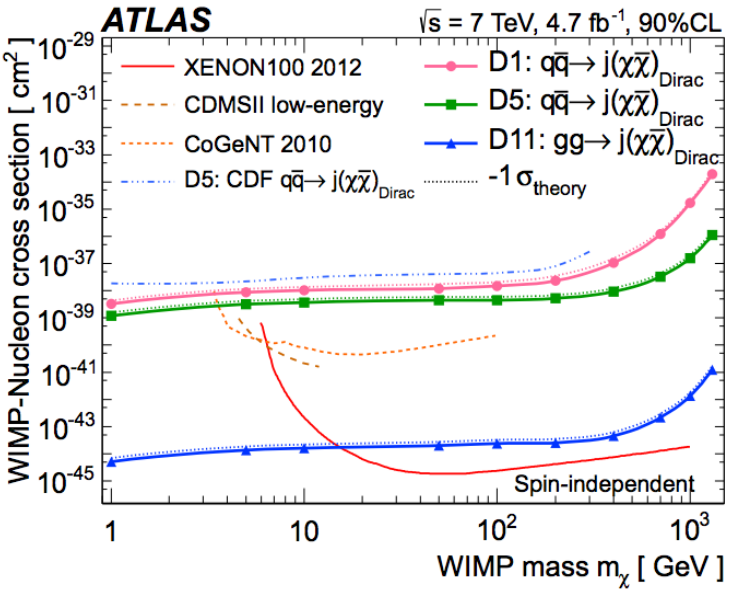


Figure 2.10: Cross section vs WIMP mass plot comparing the WIMP parameter space discounted by collider experiments vs direct searches. The results for the production of WIMPs from quark and gluon channels is shown [45].

put on the cross section of $pp \rightarrow \chi\bar{\chi} + X$ where $X$ is a hadronic jet, photon, W or Z boson. These searches have so far yielded no results that were beyond the predictions of the Standard Model. Cross section limits have also been placed based on WIMP-nucleon scattering and compared to direct detection experiments, as shown in Fig. 2.10, for a centre of mass energy run at $\sqrt{s} = 7$ TeV.

# Chapter 3

# The DEAP-3600 Detector

## 3.1 Overview

The DEAP-3600 experiment, see Fig. 3.1, is a single phase scintillation detector designed to detect spin independent WIMP-nucleon scattering. Comprised of 3,600 kg of liquid argon (LAr), the detector has a 1,000 kg active WIMP target once fiducial volume cuts are imposed. The experiment aims to have a spin independent WIMP cross section sensitivity of $10^{-46}$ cm$^2$. To achieve this, the detector was designed to minimize the impact of background. This Chapter will discuss the DEAP-3600 detector design, the main background contributions, and the background mitigation techniques.

## 3.2 General DEAP-3600 detector design

The detector design is shown in Fig. 3.1. At the centre is an acrylic vessel (AV) that will hold 3,600 kg of LAr. The vessel was manufactured to have low activity of $^{210}$Pb and studies of the acrylic purity indicate a level of $10^{-19}$ g/g of $^{210}$Pb [46]. To minimize the number of AV surface background induced events entering the signal, a fiducial volume cut on the LAr volume will be taken such that the WIMP target is approximately 1,000 kg [47]. A total of 255 PMTs that view the central volume are each separated from the acrylic vessel by

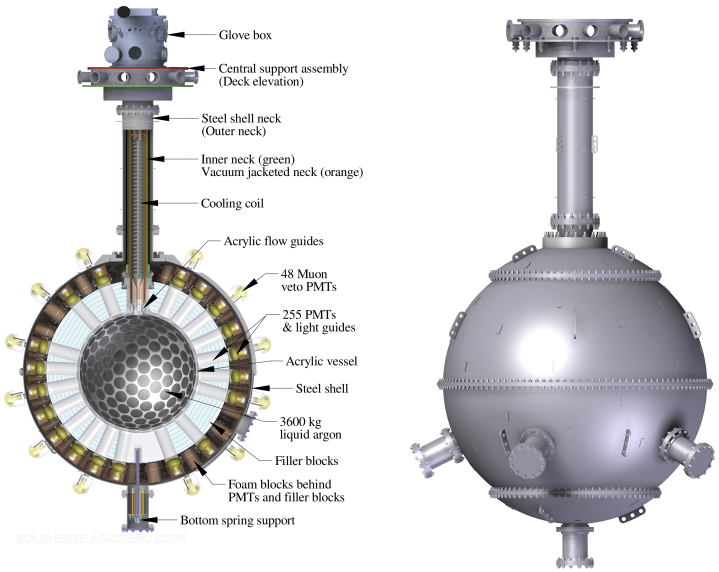


Figure 3.1: LEFT: Detector schematic. The detector is designed to reduce backgrounds in an onion layer like fashion. The setup hangs from the central support assembly. RIGHT: Schematic of detector with closed shell. This setup will be submerged in a 8 m diameter cylindrical water tank designed to provide neutron moderation. The stainless steel used for make the outer shell was sourced and manufactured in a manner to minimize the intrinsic radioactivity. The water shield with veto PMTs are not shown for illustrative purposes.

an acrylic lightguide. The space between the lightguides is occupied by filler blocks, which serve as a both neutron shield and a thermal insulator for the PMTs from the cryogenic AV. The assembly is contained inside a stainless steel shell surrounded by 48 Veto PMTs in an 8 m diameter ultra-pure water shield tank. On the top of the setup is the neck flowguide which is designed to maintain adequate cooling and flow for the liquid Argon [48]. To access the process systems there is a glove box setup at the top of the neck.

### 3.2.1 DEAP-3600 Backgrounds

A number of crucial backgrounds have the potential to impact the signals of DEAP-3600. Those include cosmic-ray induced and primordial backgrounds, which are described in the next subsections.

**Cosmic-ray induced backgrounds**

Cosmic rays are high energy particles that originate outside the Earth and are a primary source of background radiation, as they interact in the Earth's atmosphere to produce showers of secondary particles [43]. The main components of cosmic primaries are expected to be electrons, protons, alpha particles, and nuclei that are involved in stellar nucleosynthesis, including Helium, Carbon, Oxygen and Iron [49]. The decay and interaction products of some of the atmospheric secondaries can cause background events in deep site detectors, in particular muons and neutrons [49] .

For DEAP-3600 the main cosmogenic background is $^{39}$Ar, a by product of cosmic-ray induced neutrons. $^{39}$Ar is a $\beta^-$ particle emitter and has an endpoint energy of 565 keV and a half life of 269 yr, decaying to $^{39}$K via

$$^{39}Ar \rightarrow^{39} K + \beta^- + \bar{\nu}. \tag{3.1}$$

The liberation of the beta particle can cause photon production by interacting with the $^{40}$Ar scintillator. The main method to suppress this background will be trigger-level filtering and pulse shaped discrimination (PSD), discussed in section 3.3.2 [5] [50] [51]. In the future, a source of LAr with a low $^{39}$Ar concentration may be procured from underground wells that have been naturally shielded from cosmic rays [52].

As mentioned, cosmic muons are a second background concern. They can induce fast neutrons by a variety of mechanisms such as muon spallation (where a muon interaction produces a neutron by nuclear disintegration), muon elastic scattering, photonuclear reactions as a result of electromagnetic showers produced by neutrons, and secondary neutrons from the previous processes. Neutron production is problematic for the detector because they could produce nuclear recoils that mimic WIMP signals. To mitigate this background there is a water veto system that surrounds the detector (see Fig. 3.1). The water veto shield also has a set of 48 PMTs to tag muons that traverse the volume by detecting emitted Cherenkov light [53].

**Primordial backgrounds**

Primordial nucleotides are isotopes that have very long half lives (typically $> 10^8$ yr) and provide a source of background in the detector. The three main nucleotides that are of concern in the detector are $^{232}$Th, $^{238}$U and $^{40}$K. Shown in Fig. 3.2, $^{232}$Th is a continuous source of 4 MeV to 8.7 MeV $\alpha$ particles, up to 2.6 MeV $\gamma$ particles, $\beta^-$ particles, and neutrons. Similarly shown in Fig. 3.3, $^{238}$Ur is a source of 4 MeV to 7.8 MeV $\alpha$ particles and $\beta^-$ particles. The surrounding rock from the mine environment are abundant sources of the primordial backgrounds. Therefore, it is imperative that the detector is built in a very clean environment. Another source of primordial background contamination is from the detector materials themselves, making material selection an important consideration during detector construction; the PMTs typically have levels of $10^{-8}$ g/g U/Th (compared to the acrylic light guide which can be manufactured with a level of less than $10^{-13}$ g/g). Additionally, the PMT photocathode materials are a source of $^{40}$K, which itself is a $\beta$ and $\gamma$ source [5] .

A major challenge with the nucleotides are that their decay products can diffuse into the detector. If that did not happen then the situation would be relatively simple as they would just be a source of irreducible background at the detector material levels. However, if decay products diffuse into the detector it can lead to an anomalous signal source. Referring to Fig. 3.2 and 3.3 the production of $^{222}$Rn and $^{220}$Rn (by $^{238}$U and $^{232}$Th respectively) are a potential source of the discussed diffuse background. These isotopes are able to diffuse into their surrounding materials and are a source of $\alpha$ and $\beta$ radiation. The daughters of $^{220}$Rn decay relatively quickly, however $^{210}$Pb is produced from $^{223}$Rn and easily adheres to surfaces. $^{210}$Pb is a $\beta^-$ emitter in the energy region of interest ($\sim$ 61 keV) with a half life of 22 years. Additionally, the alpha decays of the intermediate daughters can be absorbed by certain nuclei and cause the emission of neutrons. To mitigate these sources it is important to keep the detector isolated from the primordial sources [50].

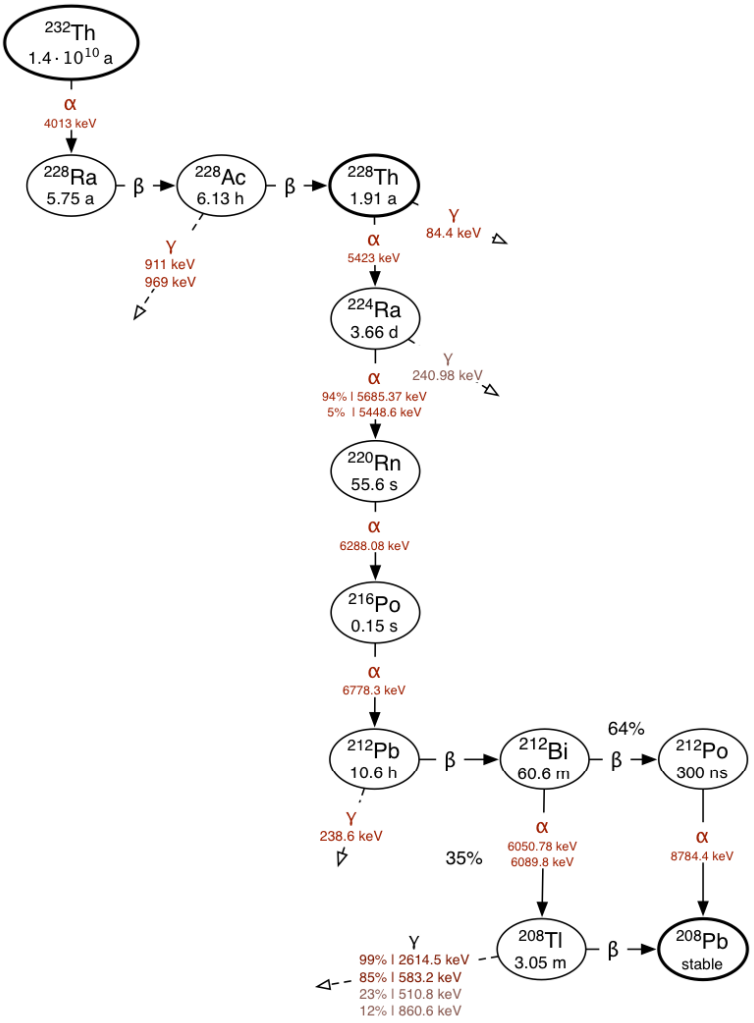


Figure 3.2: Decay chain showing decay products and energies for Thorium-232 [46].

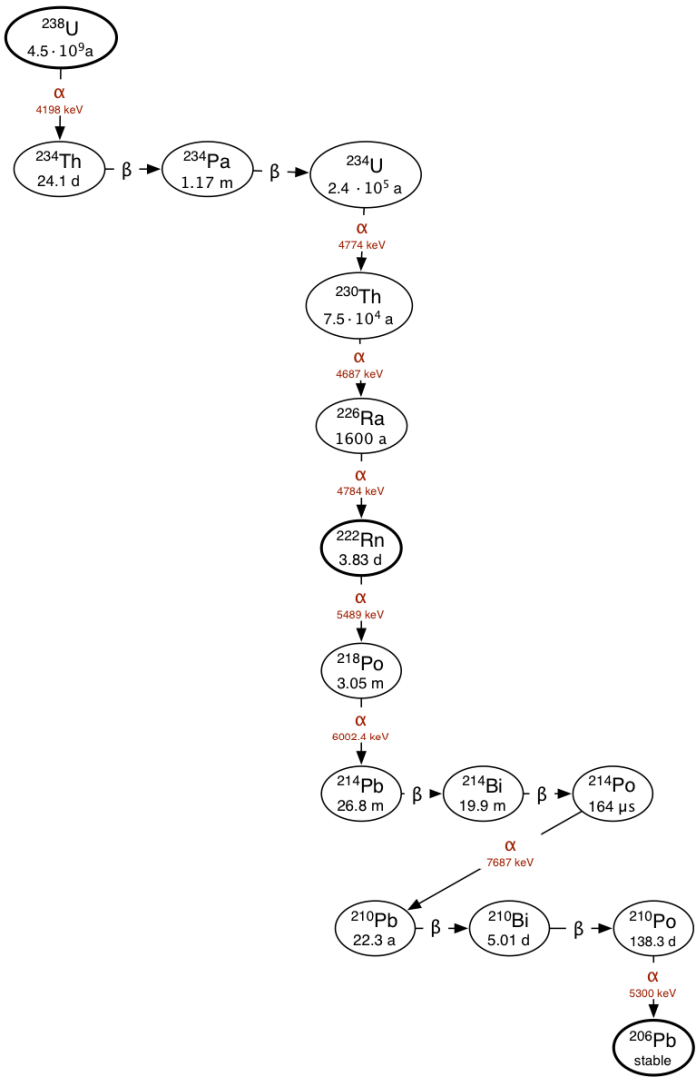


Figure 3.3: Decay chain showing decay products and energies for Uranium-238 [46].

### 3.2.2 Cryogenics

To maintain the LAr at optimal temperature there is a cooling coil setup in the detector neck connected to the cryogenic plant [48]. Liquid nitrogen (LN) is fed through the cooling coils and, since its boiling temperature is 77.36 K, the cooling power is sufficient to maintain the cryogenic requirements of the LAr (with boiling temperature 83.81 K). LN is fed from a dewar located above the neck via gravity into the cooling coils. It then boils off, is collected and returned to the dewar where it is recondenses. The LAr is held either inside a large storage dewar outside or inside the detector itself [5].

### 3.2.3 Electronics Overview

The physical layout of the electronics system is shown in Fig. 3.4. Racks I and III each contain 11 Signal Conditioning Boards (SCBs), 16 CAEN V1720 digitizer modules and two readout computers [54]. Rack II contains the main controlling computer (deap00), the CAEN V1740 module for the VETO PMTs, a trigger module and a high voltage source [55].

The electronics infrastructure is broken up into three components (see Fig. 3.4): the front end, the trigger system and the data acquisition (DAQ). Each PMT cable is fed into one of the 255 ports of SCBs, the core of the front end system. The SCBs provide several functionalities, including high voltage decoupling, waveform shaping and protection for the sensitive electronics. There are two sets of SCBs, 22 for the main 255 liquid Argon PMTs and 4 with a single slow output for the 48 veto PMTs. The 22 main SCBs have three outputs, a fast and slow signal output in addition to an analog summation of the signals (ASUM) from the 22 SCBs. The signals are input to the DAQ system for digitization, where the fast signals are fed into the 250 MS/s V1720 (8 channels, 12 bit) digitizers and the slow signals are sent to the 65MS/s V1740 (64 channels, 12 bit) digitizers. The digitizers are read out through optical links to a PCI A3818 card. The V1740s are read by 1 Front End PC and the outputs from the 32 V1720s are read by 4 frontend PCs.

The trigger decision is made by the Digitizer and Trigger Module (DTM). The DTM triggers if the ASUM passes a certain charge threshold. Once triggered the DTM provides

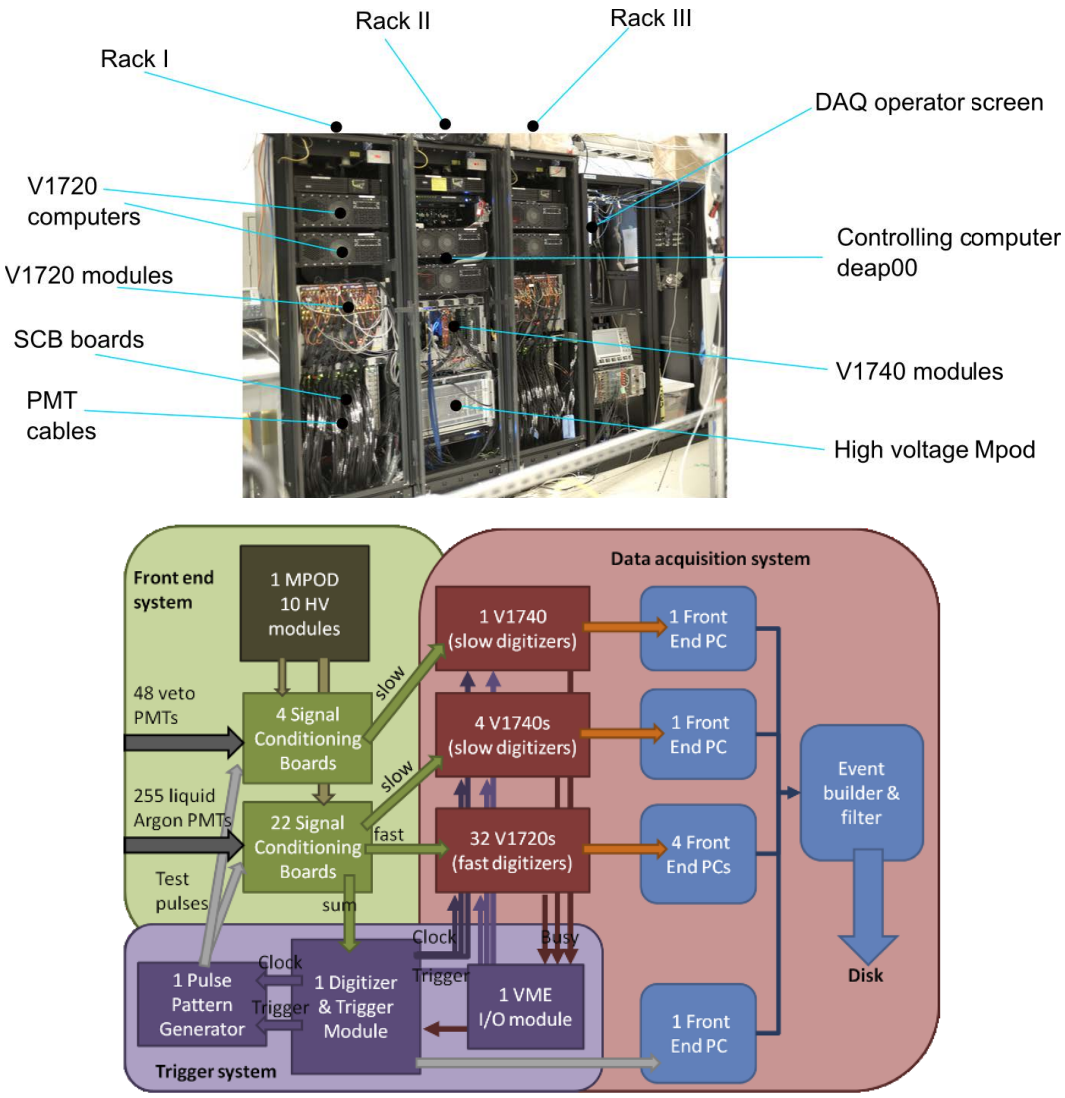


Figure 3.4: TOP: DEAP-3600 electronics layout onsite at SNOLAB. The setup sits on the deck directly above the detector. The PMT cables are fed from the detector through the deck into the electronics rack. BOTTOM: DEAP electronics schematic. This block diagram breaks the electronics system into three distinct sections, the Front End system, Data Acquisition System and Trigger System.

the timestamp information and the trigger to the digitizers. An additional role of the DTM is to also ensure that the clock and timestamps are synchronized. The DTM also outputs to a Pulse Patten Generator (PPG) when the triggered event is from a LED light injection system to measure timing offsets between the SCBs. The Versa Module Europa bus (VMEbus) module is a motherboard that enables communication between the different digitizer boards. If the digitizers are saturated with a multiple triggers, then they instruct the DTM that the digitizers are busy and not to accept more triggers until the memory buffers are cleared.

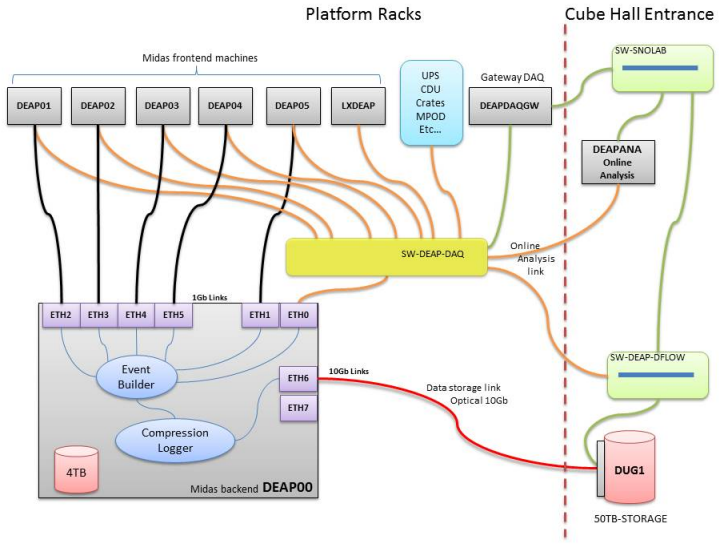


Figure 3.5: Schematic of the DEAP network infrastructure. The entire network system involves linking the electronics racks to the outside world. The Cube Hall Entrance refers to the physical location of the DEAP-3600 detector.

The DEAP network infrastructure is shown in Fig. 3.5 and physically takes the digitized signal and converts it to usable data for an offline user to analyze. The DAQ system is based on the MIDAS program which was developed at the Paul Sherrer Institute and TRIUMF [55]. The frontend computers are connected by ethernet cables to the MIDAS backend computer (deap00). The data is sent through an event builder and then sent to a 50 TB storage computer (DUG1) via a 10 GB optical link. For online analysis, the frontend machines output to a DAQ switch accessed through a gateway, called DEAPDAQGW, connected to

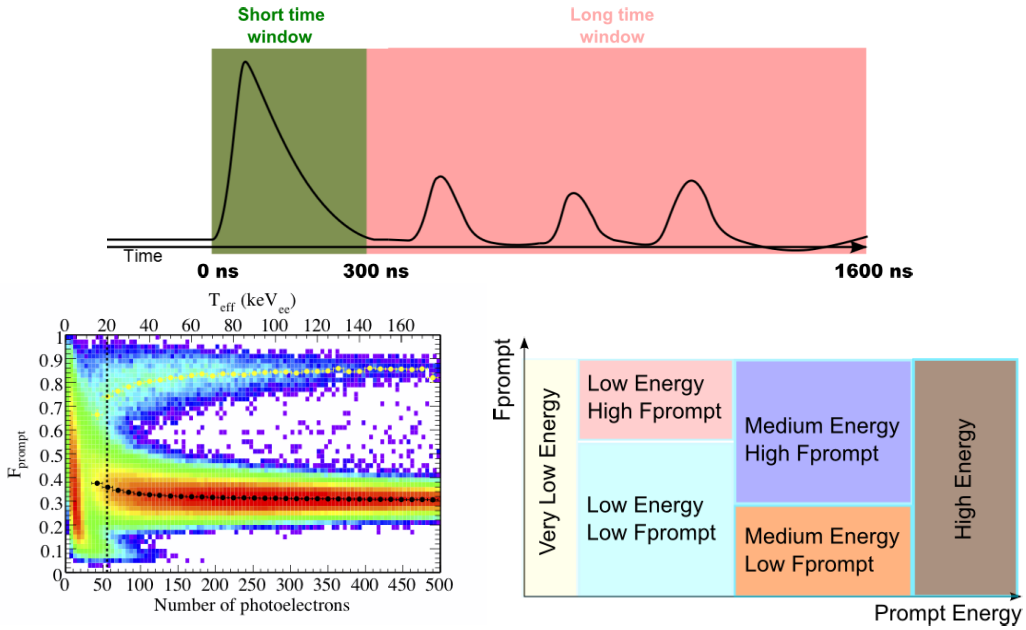


Figure 3.6: TOP: Example waveform from the DEAP I experiment. Fprompt is calculated by defining the short (300 ns) and long (∼1.6 $\mu$s) time windows and counting the charge in each window. CENTER: Fprompt vs Energy plot of the Am-Be calibration results from the DEAP I experiment. The red colored region below 40 Photoelectons (PE) are very low energy events that are dominated by dark noise and $\beta/\gamma$ recoils. The dark dotted line (between 0.3 < Fprompt < 0.4) follows the $\beta/\gamma$ recoil tail. The yellow dotted curve (at 0.6 < Fprompt < ∼0.9) follows the neutron induced recoils. BOTTOM: Fprompt vs Energy filter settings at the Eventbuilder level. The events to which the detector must be sensitive should all be caught in the Low Energy, High Fprompt box. Each of the other boxes would only have a small fraction of their events saved for calibration purposes.

a local switch onsite at SNOLAB. The switch is accessed by a local network (DEAPANA) where a DAQ operator onsite can inspect the data (see Fig. 3.4).

## 3.3 Background Event Mitigation

### 3.3.1 Trigger Level Filtering

Ideally the experiment would achieve 100% selection efficiency in the WIMP region of interest, while suppressing as much of the dominant $^{39}$Ar backgrounds as possible. This task is not trivial since the WIMP rate is expected to be less that $10^{-5}$ Hz compared to the $^{39}$Ar rate of 3,600 Hz [56]. Additionally, writing all the background $^{39}$Ar events to data would

require an extremely large amount of storage space and may be impossible to analyze on an event by event basis. There are thus two levels of data filtering to minimize the background in the WIMP region of interest. The DTM does a very coarse event selection using a physics trigger and once data taking is complete a final physics analysis can be done via pulse shape discrimination [51]. The main discrimination parameter used in the experiment is Fprompt which, as Fig. 3.6 demonstrates, is a measure of the ratio of charge $q$ in the first 300 ns of the event time window to the charge in a large 1.6 $\mu$s window, and is calculated by

$$\text{Fprompt} = \frac{\int_{0ns}^{300ns} q\,dt}{\int_{0ns}^{300ns} q\,dt + \int_{300ns}^{1600ns} q\,dt}. \tag{3.2}$$

The DTM does not explicitly calculate Fprompt, but provides a number of threshold conditions that an event must meet. This is done by the physics trigger (also known as the ADC self trigger source). If the ASUM exceeds a certain threshold, then the DTM starts recording an event. After the data are recorded for the long (300 ns to 1600 ns) and short (0 ns to 300 ns) timing window, the trigger makes a decision based on the charge calculated in the short timing window ($\mathrm{E_{short}}$), the long timing window $\mathrm{E_{long}}$) and Fprompt. For event filtering at the trigger stages, Fprompt isn't explicitly calculated. Instead 2 threshold quantities are calculated, as shown in the top plot of Fig. 3.6, the short window energy in the first 300 ns threshold, $\mathrm{E_{short}}$, and the long window energy threshold up to 1.6 $\mu$s, $\mathrm{E_{long}}$. Then, as demonstrated in the lower right hand subfigure of Fig. 3.6, two Fprompt ($\mathrm{F_{thresh1}}$, $\mathrm{F_{thresh2}}$) and two energy ($\mathrm{E_{thresh1}}$, $\mathrm{E_{thresh2}}$) threshold conditions can be defined for event characterization. When there is a physics trigger, an 8-bit trigger-type word is written, where an example word is:

$$\text{Word} : 0 \times 01 \tag{3.3}$$

$$\text{Condition} : E_{0\text{ns}-16\mu\text{s}} < E_{\text{thresh1}} \;\&\; F_{\text{thresh1}} \times E_{300\text{ns}-16\mu\text{s}} > E_{0\text{ns}-16\mu\text{s}} \tag{3.4}$$

$$\text{Word} : 0 \times 02 \tag{3.5}$$

$$\text{Condition} : E_{0\text{ns}-16\mu\text{s}} < E_{\text{thresh2}} \;\&\; F_{\text{thresh2}} \times E_{300\text{ns}-16\mu\text{s}} > E_{0\text{ns}-16\mu\text{s}} \tag{3.6}$$

The next stage of event filtering is the Eventbuilder, shown in Fig. 3.5 in the network infrastructure. The Eventbuilder contains the minimal summary of event parameters, including event type, trigger type, trigger time and event run number. A major function of the Eventbuilder is to reduce the data rate written to disk to below 5MB/s. There are 5 major event types, shown in the bottom subfigure of Fig. 3.6. The "Very Low Energy" threshold will be defined to catch mostly dark noise events. "High Energy" events are expected to be dominated by Cherenkov and alpha decays. Our window of interest include the neutron induced recoils in the "Low Energy, High Fprompt" region. The dominant $^{39}$Ar background tail, should be caught in the "Low Energy" region. The Eventbuilder will write all the raw waveforms from the "Low Energy, High Fprompt" region since those events are in the experiment's region of interest. A small percentage of events from the Low Energy region will be written to disk for trigger tuning [51] [55].

### 3.3.2 Pulse Shape Discrimination

Once a WIMP data run is complete, the filtered Fprompt vs charge distribution should resemble the DEAP I data run as shown in Fig. 3.7. In the DEAP I data runs $1.23{\times}10^8$ events were analyzed. The analysis showed that the upper limit discrimination power between the $^{39}$Ar background in the 44 keV$_{\text{ee}}$ - 89 keV$_{\text{ee}}$ energy range was $< 2.8 \times 10^{-8}$ with 90 % confidence [51]. For DEAP-3600 the projected discrimination power is at the level of $10^{-10}$, meaning the $^{39}$Ar background and WIMP region of interest events can be discriminated to a much higher degree. After a multi year exposure the number of events in the WIMP region of interest may be plotted as a function of time and an additional annual modulation test can be made [51] [57].

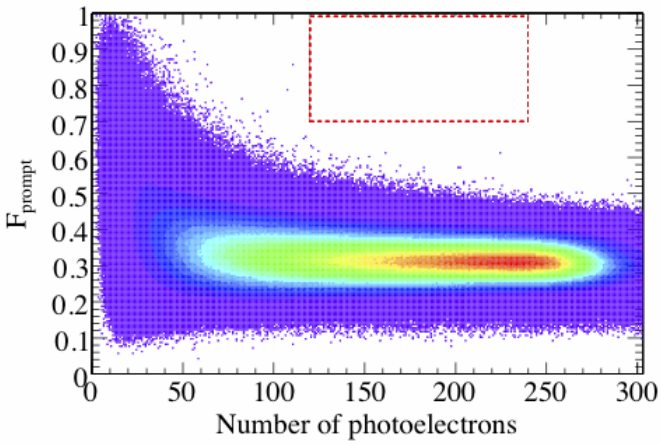


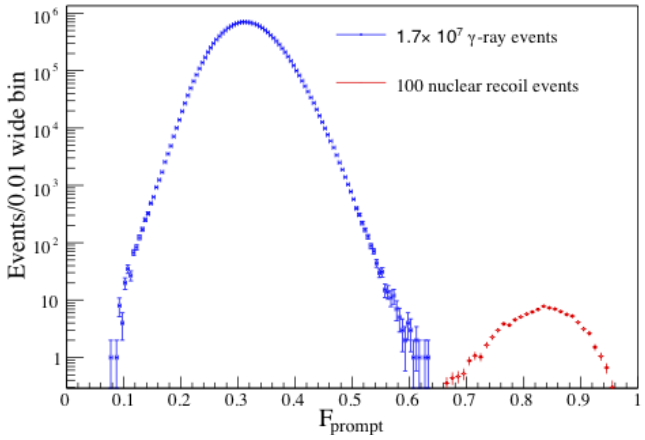


Figure 3.7: TOP: Fprompt vs energy distribution from the DEAP I data run. Most of the events were $\beta/\gamma$ induced recoils. The dotted red curve represents nuclear recoils in the WIMP region of interest. BOTTOM: A 1D projection of Fprompt from the diagram above. There are some overlap events between the $\beta/\gamma$ induced recoils and nuclear recoils. This is accounted for by fitting the Fprompt distributions to Gaussians to resolve the statistical likelihood that an event was seeded from one type of event or the other.

# Chapter 4

# Characterization of the DEAP-3600 Photomultiplier Tubes

## 4.1 Overview

This Chapter describes the methodology applied to characterize the Hamamatsu R5912 PMTs used in DEAP-3600, in particular the primary features of afterpulsing and dark noise. It begins with an overview of PMT operation and discusses how a single scintillation photon can produce a measurable signal. There is a review of measurements conducted by Hamamatsu of the causes of temperature response and potential afterpulsing. Also reviewed are afterpulsing studies completed for the Double Chooz experiment, who used similar PMTs to DEAP-3600. There will be an explanation of our methodology used in afterpulsing and dark noise characterization for a single PMT. The Chapter will close with a study of the charge distributions of different groups of late pulses for a single PMT and a study of whether SPE afterpulsing is equivalent to multiple PE afterpulsing.

## 4.2 Photomultiplier Tube operation

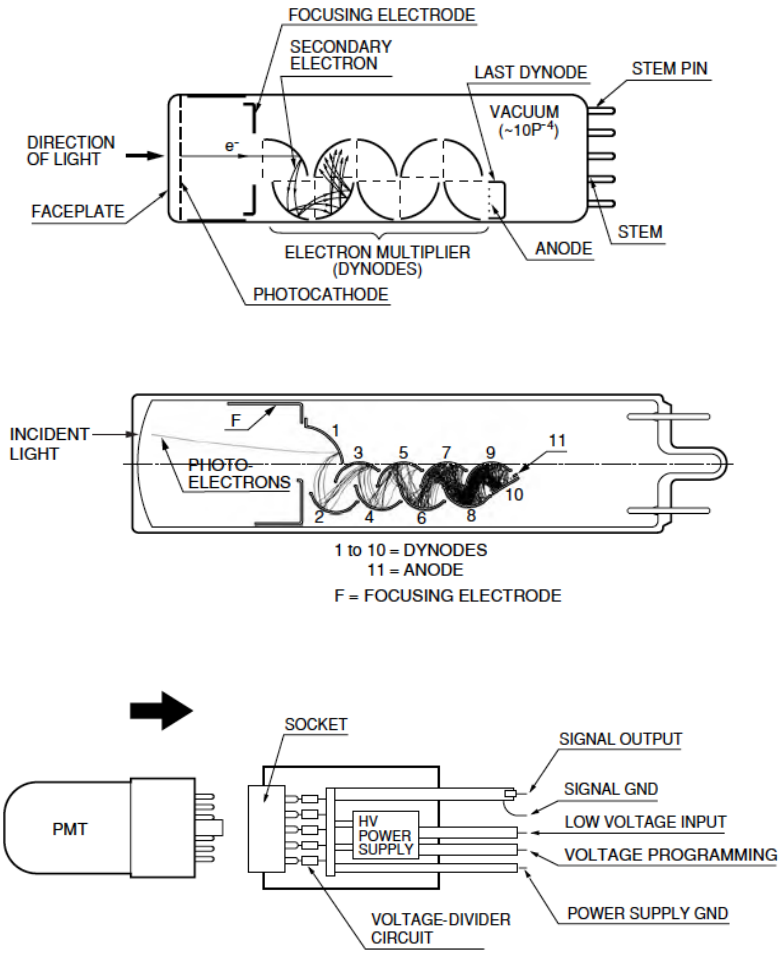


Figure 4.1: TOP(from [58]): Internal setup of a typical PMT. Scintillation light enters, passing through the faceplate and striking the photocathode. Liberated photoelectrons are then multiplied by the dynode stages and are collected at the anode. CENTER: This subfigure shows in more detail the process of electron multiplication at each of the dynode stages in a setup similar to the PMTs used in DEAP 3600. BOTTOM: Schematic showing the PMT plugged into its socket [58].

The purpose of a PMT (see Fig. 4.1) is to detect incident light and produce a detectable electrical signal [58]. Light enters the device after passing through the faceplate, which for the Hammastu R5912 PMTs is made from borosilicate glass. Incoming photons strike the photocathode layer deposited on the inner surface of the faceplate, causing the emission of

photoelectrons via the photoelectric effect [58]. Photocathodes are semiconductors and the emission of the photoelectron can be understood by looking at the photocathode from the semiconductor band gap model [59]. As demonstrated in Fig. 4.2, for a photoelectron to be released, the incoming photon has to have enough energy ($h\nu$) to overcome the photocathode work function $\psi$. Here, $\psi$ is defined as the difference between the vacuum-level and the Fermi-level of the photocathode. The vacuum-level is determined by the electron affinity of the material which is a forbidden energy gap that cannot be occupied by electrons and separates the conduction and valence band. The ability of a material to emit photoelectrons is typically expressed in terms of the quantum efficiency, which physically describes the ratio of output electrons to incident photons [60]. The photocathode used in the Hamamatsu R5912 PMTs is a bialkali with a quantum efficiency of 38% [56].

Once the photoelectrons are liberated from the photocathode stage, they are accelerated through a focusing electrode and then the number of photoelectrons are multiplied at the electron multiplier stage. The electron multiplier stage is made up of a series of dynodes that are substrates coated with a secondary emissive material. The operating voltage at each dynode stage is optimized to enable an electron multiplication factor of about 10. Thus, ideally for the 10-stage dynodes in the Hamamatsu R5912 there should be a total secondary electron production of $10^{10}$ for a single incident photoelectron [56]. The secondary electron collection finally occurs at the anode.

The final stage of the PMT assembly is the socket that is shown in Fig. 4.1. The socket contains the high voltage connections for each of the dynode states as well as the signal output. Finally, the PMT base contains a voltage divider circuit to ensure that the dynodes potentials are set correctly.

## 4.3 PMT noise sources

There are a number of potential sources of noise that can affect the performance of a PMT. The most common are dark currents (dark noise) and afterpulses. Dark current is a measurable electronic current that is not induced from an incident photon. Afterpulses

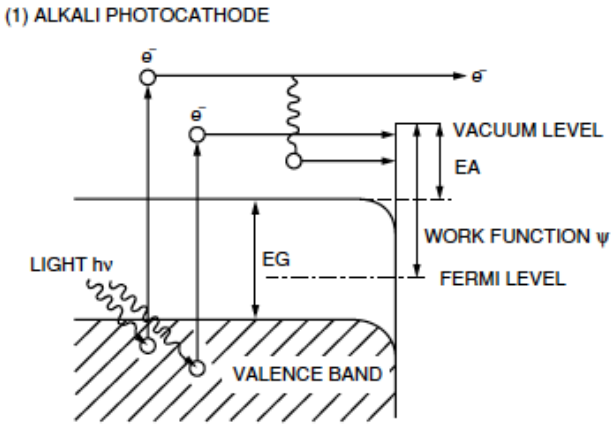


Figure 4.2: An energy-level diagram for the process of photoelectron emission from an incident photon with energy $h\nu$ striking a photocathode [58] .

are pulses that typically occur after the single photoelectron induced pulse. These are typically caused by residual gas ions that are ionized by the accelerating electrons between the first and second dynode [61]. The residual gas ions slowly drift and eventually strike the photocathode, resulting in the release of more electrons that can be multiplied.

### 4.3.1 Dark Noise

There are a number of potential causes of dark current, such as thermionic emission, leakage currents, scintillation from the glass envelope or electrode support materials, ion feedback, background radiation and field emission [58]. The materials that make up the photocathode and dynode stages must have a low work function for efficient production of photoelectrons and secondary electrons respectively. The current generated $\mathrm{i_{dark}}$ is given by the Richardson equation [58] where,

$$\mathrm{i_{dark}} \propto \mathrm{T}^{5/4}\mathrm{e}^{-\frac{\mathrm{e}\,\psi}{\mathrm{k\,T}}}. \tag{4.1}$$

Here $e$ is the electron charge, $k$ is Boltzman's constant, $T$ is absolute temperature and $\psi$ is the material work function [60].

Scintillation from the glass envelope, as explained below, is an additional source of dark

current that is difficult for the end user to reduce. The photocathode typically has a high negative voltage applied to it and is housed in a metal case held at ground. This can cause stray electrons to strike the glass envelope and produce scintillation light that can then be picked up by the photocathode. This effect may be reduced by requiring there be only a small amount of scintillating material in the glass [58].

If the PMTs are operated at higher than recommended voltages, a dark current due to field emission can be produced. The presence of a strong electric field can cause the emission of electrons from the dynode stages. Additionally, the presence of potassium oxide ($K_2O$) in the PMT glass means that there is a natural source of $^{40}K$ providing photons that can strike the photocathode. Additionally, cosmic rays are another source of dark noise, but cosmic rays may be mitigated as discussed in Section 3.2.1.

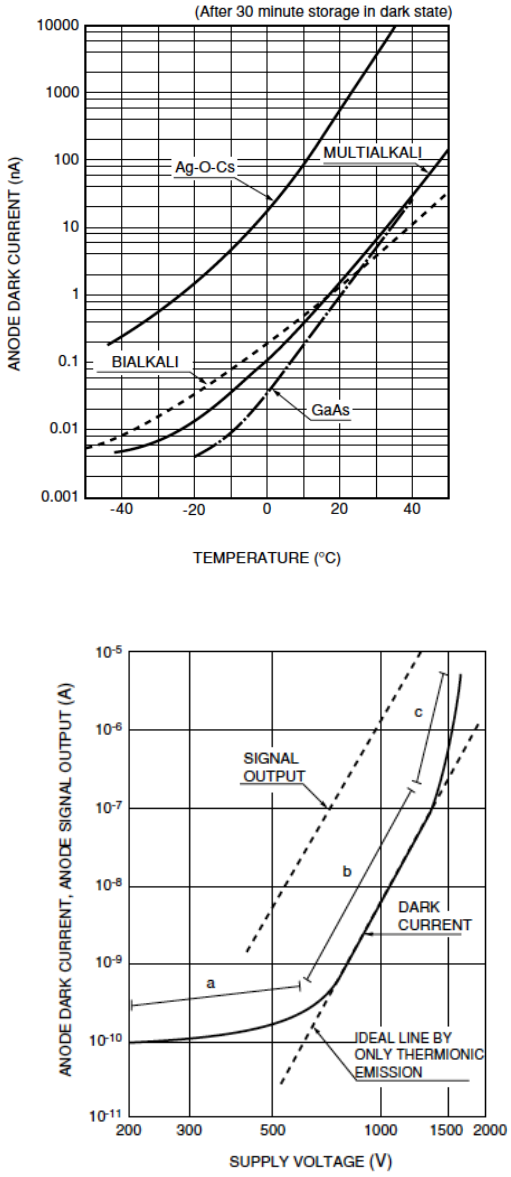


Figure 4.3: TOP: Measurements of the dark current variation as a function of PMT temperature after 30 minutes of storage in a dark state. Several different PMTs were tested, each with different photocathode materials. For bialkali photocathodes like those in DEAP-3600, there is a decrease of anode dark current from 1.5 nA at 25 $^o$C to 0.08 nA at -20 $^o$C. BOTTOM: A voltage scan of dark rates with a Hamamatsu test PMT [58].

A significant concern for DEAP-3600 is the changes in the dark current as a function of applied voltage and operating temperature. Fig. 4.3 illustrates the general behavior of

the dark current variation as a function of voltage for a test Hamamatsu R6095 PMT and as a function of temperature for a variety of PMTs. Based on engineering specifications for the DEAP-3600 detector, the PMTs are expected to operate at about $\approx$ 250 K (-20 $^{o}$C) and not to be exposed to temperatures below 240 K (-30 $^{o}$C). Preliminary studies of the R5912 suggest that the dark rate could decrease between 1 to 1.5 orders of magnitude for a temperature decrease from room temperature to 250 K. Fig. 4.3 can help illuminate how the dark rate will vary during the detector cool-down. According to Fig. 4.3 the dark rate (for PMTs with bialkali photocathode) should decrease by 2 orders of magnitude for the cooldown temperature of about 240 K [62].

The operating voltage is not expected to be varied when operating the DEAP-3600 PMTs. The operating voltage must be set carefully because, as Fig. 4.3 shows, incorrect settings can result in significant variations in the dark current rates [56].

### 4.3.2 Afterpulsing

Afterpulsing is a challenge because it can be the cause of anomalous physics triggers and degrade the pulse shape discrimination. It is therefore important to understand the magnitude and timing of afterpulses to mitigate this. Afterpulses are typically classified in two distinct groups, short delay afterpulses (typically one to several hundred ns) and long delay afterpulses (several hundred ns to tens of $\mu$s) [63]. Short delay afterpulsing is typically caused by elastic-scattered electrons incident on the first dynode, while long delay afterpulses are caused by residual ion feedback in the PMT [58]. During the electron multiplication stage electrons can ionize residual gases inside the PMT leading to the production of a positive ion. These positive ions slowly drift toward the photocathode and can cause the production of many photoelectrons [64].

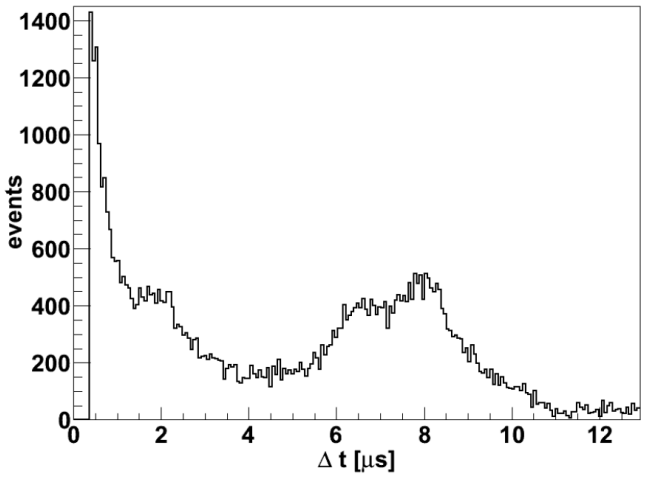


Figure 4.4: An afterpulsing spectrum measured by the Double Chooz experiment using a Hammatsu R7081 PMT [59]. Their dataset shows late pulses starting at 500 ns. There are several prominent peaks beyond 500 ns, between 1.8 $\mu$s to 2 $\mu$s and between 6 $\mu$s to 9 $\mu$s [63]. It is likely that the afterpulse between 6 $\mu$s to 9$\mu$s [63] is induced by Cs ions. The large peak at 500ns is likely due to Coulomb backscattering.

There have been a number of studies designed to try and understand which residual gas ions are responsible for the afterpulsing behavior. The afterpulsing spectrum of the Hamamatsu R7081 PMT, used in the Double Chooz experiment, is shown in Fig. 4.4 [63]. Four prominent afterpulse peaks are observed between 5 $\mu$s to 7 $\mu$s occurring due to several residual gas ions [64]. The ions are identified by calculating their transit time, $\Delta t$, using the electric potential distribution inside a hemispherical PMT. The calculated transit time assumes a quadratic potential such that,

$$\delta t = \frac{4}{\pi}\sqrt{\frac{2m}{qV_0}}L, \tag{4.2}$$

where $V_0$ is the electric potential at the first dynode, $q$ and $m$ are the ion charge and mass, respectively, and L is the distance to the photocathode. Table 4.1 shows the observed afterpulse and the associated ions. This produces an interesting metric for comparison to DEAP-3600 data because the R7081 has a similar dynode structure, physical dimension and operating voltage as the R5912.

| Mean $\langle t \rangle$ ($\mu$s) | Possible Ion |
|---|---|
| 0.52 | $H^+$ |
| 2.10 | $CH_4$ |
| 4.90 | $N_2{}^+$ |
| 6.30 | $Cs^+$ |
| 7.90 | $CO_2$ |

Table 4.1: Table of potential sources of afterpulse ions calculated for the Hamamatsu R7081 [63].

## 4.4 Characterizing the noise spectrum from DEAP-3600

This section describes how the charge and timing information for a typical DEAP-3600 pulse is characterized by the Derivative Single Pulse (DSPE) processor and how the data are written into the Reactor Acquisition Tool (RAT) data structure. This section also covers how SPE-like pulses are found using the Polya fit method [65] and how the late pulsing spectra is constructed using a 2D histogram containing the late pulse charge and time. Results are presented comparing the late pulsing response from an external photoelectron and a dark noise photon. Also presented is an analysis of the afterpulsing charges observed in DEAP-3600.

### 4.4.1 Derivative Single Photoelectron Processor

The physical quantities required to characterize the afterpulsing and dark noise are the charge and time of a triggered pulse. A typical DEAP data stream is shown in Fig. 4.5. A pulse is identified here by a Pulsefinder algorithm called the DSPE processor [66]. When a hit is triggered, if the pulse derivative crosses a certain threshold the start of the event is set to 8 ns prior. The end of the pulse is defined as the point where the voltage drops below the baseline and the derivative is small. Fig. 4.5 shows how DSPE separates pulses in time. The pulse is then fit for the number of single photoelectrons using a maximum likelihood. A number of observables can then computed for each pulse including the charge information, found by integrating the voltage in each time window and converting to pC. For each waveform block, several times are computed: the time when the derivative threshold is

passed, the peak of the time distribution (which should align with the pulse trigger time), and the left and right edge of the triggered pulse distribution [66].

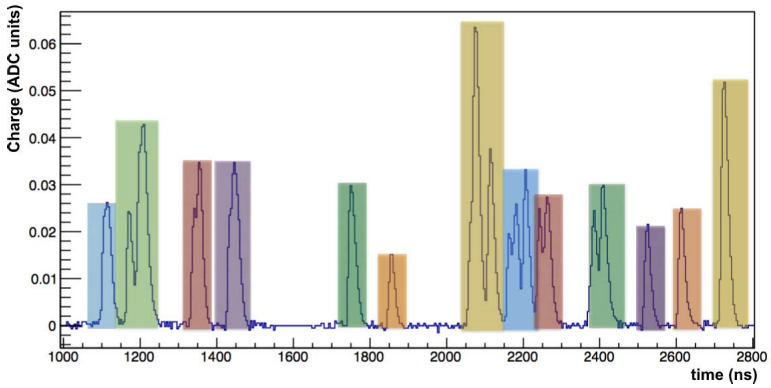


Figure 4.5: Example of raw data pulses that the DSPE processor is designed to identify. Each of the identified pulses in a given timing window are highlighted [66].

### 4.4.2 RAT data structure

The observables calculated by the DSPE processor are populated inside the RAT data structure [55]. RAT is a data analysis framework that was developed for the Braidwood collaboration for modeling the behavior of a liquid scintillator volume surrounded by PMTs. The data written from the experiment are also populated in the RAT data structure including the calibrated data and raw event data. The calibrated data object contains PMT hit information for up to 255 PMTs with the charge and time observables calculated by the pulse data populated by the DSPE processor. The data structure is easily accessed by ROOT macros [55].

### 4.4.3 Single photoelectron selection

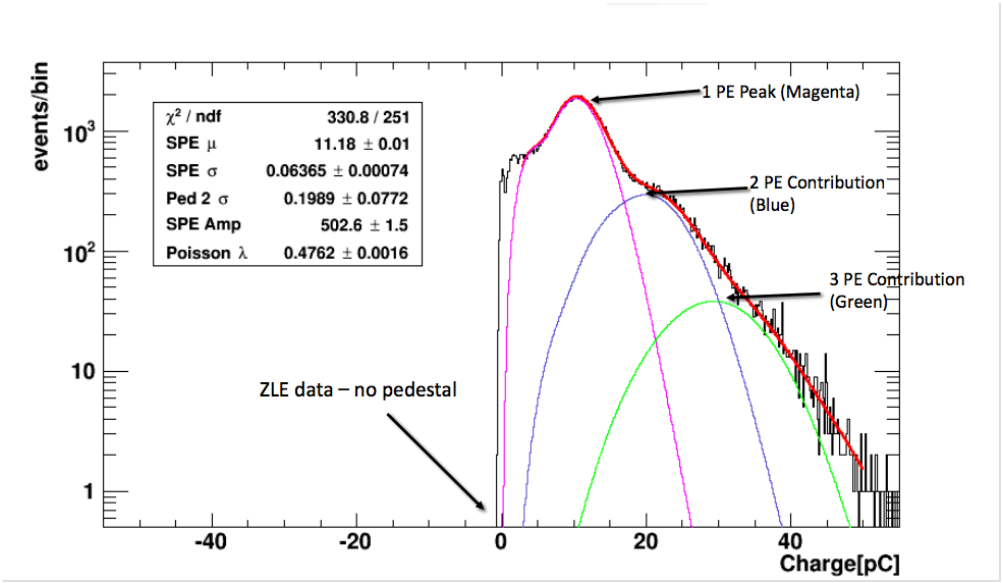


Figure 4.6: TOP: Example of a charge histogram from a DEAP-3600 dark run with sample photoelectron identification by fitting the charge distribution for a particular PMT. The charge threshold for the primary pulse is built using the fit parameters from these histograms [65].

The method to evaluate the afterpulsing and dark noise presented here utilizes single photoelectron (SPE)-like hits. This is done by looking at the charge histogram for a single PMT. In a typical charge distribution, near 0 pC there is a pedestal that is automatically subtracted in DEAP data sets. To ensure accurate SPE selection, a charge threshold is set for single pulses. The threshold is determined by extracting the SPE limits from a multiple PE event, as shown in Fig. 4.6. A SPE fit function model, based on a Polya distribution [65], and the full fit function, based on a convolution of the SPE fit function and a pedestal fit function are employed. The number of photoelectrons in an event can be estimated from this method and it is used to build the SPE threshold condition [65].

### 4.4.4 $\Delta$t spectrum and fit function

To quantify the afterpulsing and dark noise, a fit of the noise ($\Delta t$) spectrum from a SPE-like hit is performed. The first two pulses in the timing window are counted to mitigate the

effects of follow-up afterpulsing. There are several steps to making the $\Delta t$ spectrum. For a pulse to be identified as having physical afterpulses it has to pass a number of tests. To ensure that a seed SPE pulse can produce distinguishable afterpulses it has to occur at a time where a second pulse would not be missed. For dark data runs this means that if the data were taken with a 200 $\mu$s timing window then the first pulse must occur in the first 100 $\mu$s. If the data set is taken with a (445 nm) laser source injecting light into the detector, then the first pulse must occur after the laser pulse to be a physical afterpulse. If these conditions are met, and there is a secondary pulse, then the time difference, $\Delta t = t_{\text{secondary pulse}} - t_{\text{spe pulse}}$ can be calculated.

A 2D histogram is produced for each PMT containing the charge of the secondary pulse versus $\Delta$t, which may be projected in $\Delta$t to obtain a 1D $\Delta$t spectrum as shown in Fig. 4.7. There are several interesting features in this histogram. There are a strong correlation of SPE-like hits before 100 ns as shown in Box 1. These hits are likely to be due to Coulomb backscattering [64]. There are a number of highly correlated hits between 100 ns and 9 $\mu$s that are physical afterpulses. In Box 2 there is a line of multiple PE hits at approximately 350 ns. In Box 3 there are a number of sub-SPE hits. Box 5 contains a number of correlated SPE hits and a sub-SPE tail. Boxes 4 and 6 contain a number of correlated hits in time and charge. The hits in Box 7 occur at $\Delta t$ beyond 10 $\mu$s and are just dark noise hits. There are also randomly distributed multiple PE charged dark noise hits throughout the plot.

This spectrum may be normalized by scaling the 1D $\Delta t$ distribution with the number of single pulses. The distribution is then fit so that the physical parameters, such as dark noise rate and afterpulsing probability, can be calculated. The dark noise tail observed in Fig. 4.7 is fit to an exponential decay since its process is measured to be dictated by Poisson statistics, where the probability for finding a dark noise pulse at time $t$(ns) is $p_{DN}$ and the probability of finding no dark noise pulse is $\overline{p_{DN}}$, given by

$$p_{\text{DN}} = R \tag{4.3}$$

$$\overline{p_{\text{DN}}} = e^{-Rt} \tag{4.4}$$

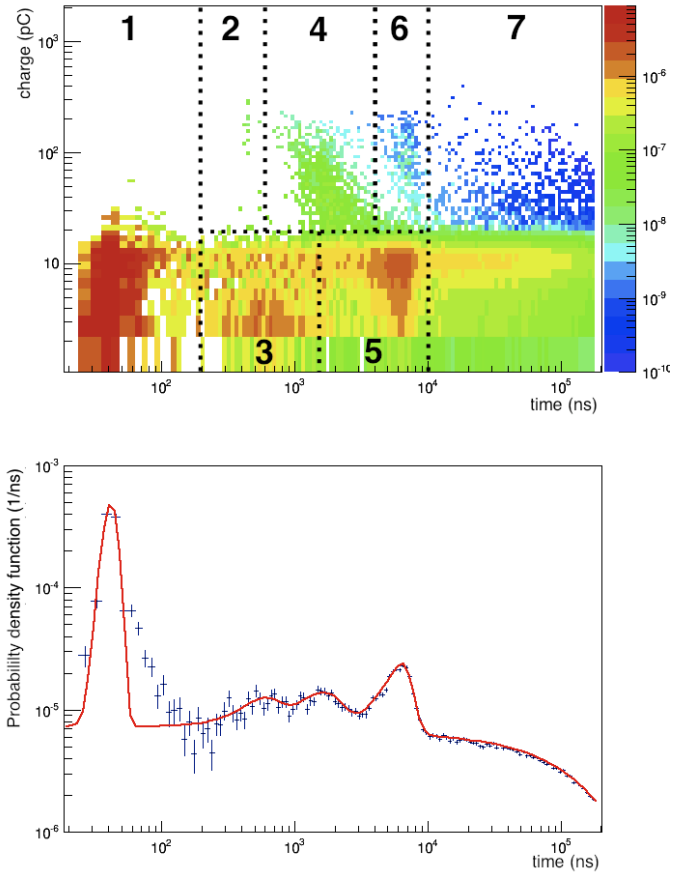


Figure 4.7: TOP: charge versus $\Delta t$ response of PMT 100 from a dark noise run. The main afterpulsing features are segmented into 7 regions. BOTTOM: A fit of the 1D projection of the charge versus $\Delta t$ histogram. There are four distinct features: The earliest afterpulse represented by a large pulse peaked at 60 ns, a group of transient afterpulses between 200 ns and 3 $\mu$s and a prominent afterpulse at 6.2 $\mu$s. For $\Delta t > 10$ $\mu$s the pulses are dark noise.

Here $R$ is the dark noise rate in units of 1/ns. The afterpulses are fit with a Gaussian distribution and the probability per ns to obtain an afterpulse $p_{AP}$ and the probability of finding no afterpulse $\overline{p_{\mathrm{AP}}}$ are given by,

$$p_{\mathrm{AP}} = \nu_{\mathrm{AP}} \frac{1}{\sigma\sqrt{2\pi}} e^{-\frac{1}{2}(\frac{t(\mathrm{ns})-\tau}{\sigma})^2} \tag{4.5}$$

$$\overline{p_{\mathrm{AP}}} = 1 - \frac{1}{2}\nu_{AP}\left(1 + \mathrm{Erf}\left(\frac{t(\mathrm{ns})-\tau}{\sigma}\right)^2\right). \tag{4.6}$$

Here $\nu_{\mathrm{AP}}$ is the afterpulse rate, $\tau$ is the afterpulse time and $\sigma$ is the afterpulse variance. The full fit function is completed by calculating the probability of producing a single afterpulsing $p_{\mathrm{SP}}$ and multiple afterpulses $p_{\mathrm{TOT}}$,

$$p_{\mathrm{SP}} = \overline{p_{\mathrm{DN}}}\ \overline{p_{\mathrm{AP}}}\ (p_{\mathrm{DN}} + p_{\mathrm{AP}}) \tag{4.7}$$

$$p_{\mathrm{TOT}} = \prod_{i=0}^{i\leq n} \overline{p_{\mathrm{DN}}}\ \overline{p_{\mathrm{AP}}}[i]\ (p_{\mathrm{DN}} + \sum_{i=0}^{i\leq n} p_{\mathrm{AP}}[i]) \tag{4.8}$$

Equation 4.7 is based on the assumption that if there is a pulse at some time it must either be a dark noise pulse and not an afterpulse or vice versa. Fig. 4.7 shows the fitted 1D $\Delta t$ distribution and the corresponding fit parameters that provide the afterpulsing probabilities and times and the dark noise rate.

Using this fit function the physical parameters can be estimated for a single PMT. Table 4.2 shows the fit values such as dark noise rate and the afterpulsing times and probabilities. The fitted dark noise rate of 7.52 kHz ± 0.19 kHz is slightly higher than the normal operating dark rate of 6 kHz as stated by the Hamamatsu data sheet [59]. However, the value is well below the maximum observed rate of 12 kHz. Between 100 ns to 10 $\mu$s there were four afterpulses fitted at 0.48 $\mu$s ± 0.05$\mu$s, 1.54 $\mu$s ± 0.11 $\mu$s, 5.91 $\mu$s ± 0.37 $\mu$s and 6.64 $\mu$s ± 0.18 $\mu$s, with 2.2 %, 3.8 % , 1.2 % and 0.2 % incidence respectively. This means that there is a total afterpulsing probability of 7.5 % predicted for this particular PMT. This value is higher than the typical afterpulsing rate of 2 % measured by Hamamatsu but is lower than the measured 10 % maximum. This rate is consistent with previous

measurements performed by the DEAP-3600 collaboration.

There are some differences between our afterpulsing spectrum and that measured by Double Chooz (discussed in the previous section). There are some broad features that agree such as the afterpulsing peaks at 6 $\mu$s to 9 $\mu$s and the afterpulsing peak at 2 $\mu$s. The Double Chooz early afterpulsing measurements measured a high number of counts at 0 $\mu$s to 1 $\mu$s whereas we see a distinct peak at 50 ns and transient afterpulsing between 200 ns and 1 $\mu$s.

| Fit Parameter | Fit value |
|---|---|
| Dark Noise rate (kHz) | 7.52 ± 0.19 |
| | |
| Afterpulse 1 probability (%) | 2.24 ± 0.15 |
| Afterpulse 1 $\tau$ ($\mu$s) | 6.64 ± 0.18 |
| Afterpulse 1 $\sigma$ ($\mu$s) | 0.93 ± 0.23 |
| | |
| Afterpulse 2 probability (%) | 3.79 ± 1.43 |
| Afterpulse 2 $\tau$ ($\mu$s) | 5.91 ± 0.37 |
| Afterpulse 2 $\sigma$ ($\mu$s) | 1.78 ± 0.35 |
| | |
| Afterpulse 3 probability (%) | 1.24 ± 0.16 |
| Afterpulse 3 $\tau$ ($\mu$s) | 1.54 ± 0.11 |
| Afterpulse 3 $\sigma$ ($\mu$s) | 0.70 ± 0.10 |
| | |
| Afterpulse 4 probability (%) | 0.20 ± 0.11 |
| Afterpulse 4 $\tau$ ($\mu$s) | 0.48 ± 0.05 |
| Afterpulse 4 $\sigma$ ($\mu$s) | 0.15 ± 0.08 |

Table 4.2: Afterpulsing and dark noise fit output of PMT 100.

## 4.5 Dark datasets versus AARF datasets comparison

To test whether the afterpulsing and dark noise spectra from a photoelectron and from a dark noise photon are the same, a comparison between an Aluminum and Acrylic Reflector and Fiber optic system (AARF) dataset and a dark run dataset was performed. The AARF is a non-invasive optical calibration system physically constituting of 20 optical fibres connected to an aluminum coated acrylic stud. These fibres are bonded to the acrylic light guides such that 80 % of the light is directly incident to the corresponding PMT and about 20 % is reflected from the PMT face into the rest of the detector, providing a source of

photoelectrons.

Fig. 4.8 shows the charge versus $\Delta t$ histogram and the corresponding 1D $\Delta t$ projection for an AARF and dark data run. Both 2D histograms retain the same major afterpulsing features, albeit with different statistics. The fitted $\Delta t$ projections also share the same major features, with a large initial pulse below 100 ns, three prominent afterpulses and a dark noise tail.

| Fit Parameter | AARF run fit value | Dark run fit |
|---|---|---|
| Dark Noise rate (kHz) | 5.99 ± 0.29 | 5.57 ± 0.54 |
| | | |
| Afterpulse 1 probability (%) | 0.59 ± 0.31 | 0.36 ± 0.19 |
| Afterpulse 1 $\tau$ ($\mu$s) | 6.76 ± 0.11 | 6.87 ± 0.13 |
| Afterpulse 1 $\sigma$ ($\mu$s) | 0.40 ± 0.17 | 0. 28 ± 0.11 |
| | | |
| Afterpulse 2 probability (%) | 5.36 ± 0.35 | 4.68 ± 0.29 |
| Afterpulse 2 $\tau$ ($\mu$s) | 6.00 ± 0.09 | 6.20 ± 0.08 |
| Afterpulse 2 $\sigma$ ($\mu$s) | 1.42 ± 0.08 | 1.32 ± 0.07 |
| | | |
| Afterpulse 3 probability (%) | 1.35 ± 0.15 | 1.03 ± 0.12 |
| Afterpulse 3 $\tau$ ($\mu$s) | 1.66 ± 0.09 | 1.85 ± 0.07 |
| Afterpulse 3 $\sigma$ ($\mu$s) | 0.68 ± 0.09 | 0.53 ± 0.07 |
| | | |
| Afterpulse 4 probability (%) | 0.12 ± 0.06 | 0.11 ± 0.04 |
| Afterpulse 4 $\tau$ ($\mu$s) | 0.52 ± 0.05 | 0.45 ± 0.03 |
| Afterpulse 4 $\sigma$ ($\mu$s) | 0.10 ± 0.05 | 0.07 ± 0.028 |

Table 4.3: AARF versus Dark run afterpulsing and dark noise fit output of PMT 200.

The overlay of the AARF and Dark $\Delta$t distributions, as shown in Fig. 4.8 have a good qualitative agreement. To quantify the agreement, the fit parameters from the $\Delta$t fits are shown in Table 4.3. The dark rates for the two datasets agree to within $1\sigma$ and were computed to be about 6 kHz. Afterpulse 1 and 2 peak times agree for both data sets to within $1\sigma$. The peak times for afterpulse 3 and 4 agree within $2\sigma$.

## 4.6 Afterpulse Charges

To understand the types of charge distributions contributed to by each afterpulsing region, the charge versus $\Delta t$ plot was segmented into 5 different regions, as shown in Fig. 4.9. The

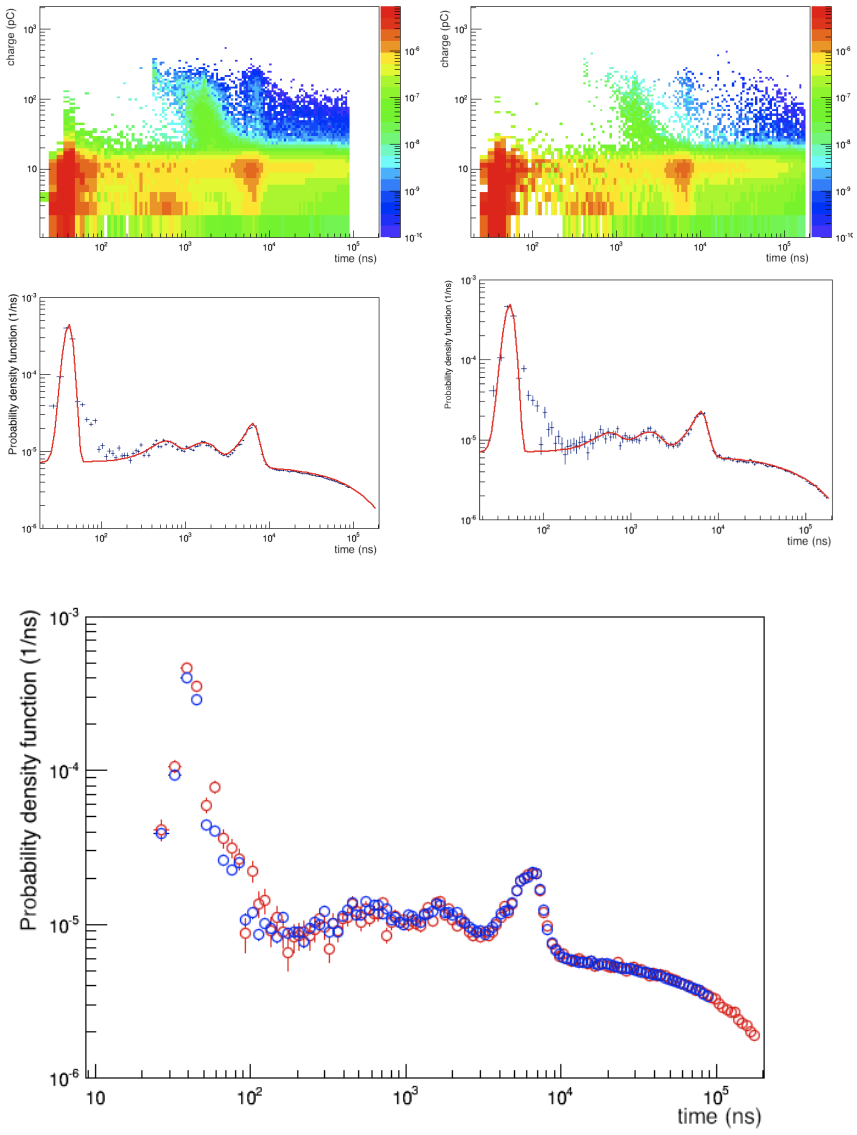


Figure 4.8: TOP LEFT and CENTER LEFT: Charge versus $\Delta$t histogram from an dark data run and the corresponding 1D $\Delta$t projection. TOP RIGHT and CENTER RIGHT: Charge versus $\Delta$t histogram from an AARF data run and the corresponding 1D $\Delta$t projection. BOTTOM: Overlay of $\Delta$t histogram from dark (blue) and AARF (red) data runs.

color axis represents the number of pulses in that particular bin. Region 1 (R1) contains the Coulomb backscattered events. Region 2 (R2), Region 3 (R3) and Region 4 (R4) contain the pulses responsible for the possible ion induced afterpulses. Region 5 (R5) contain the dark noise pulses. The 1D charge histograms were produced by projecting the charge distributions within the given range of time bins. There are high charge dark noise pulses in Region 4. It is necessary to subtract the high charge dark noise contribution from Region 3 since it contains a large number of high charge pulses that may be due to afterpulsing of dark noise.

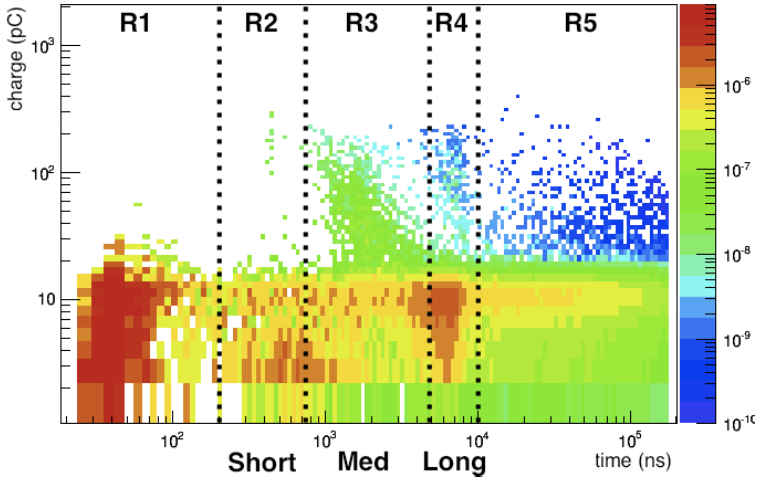


Figure 4.9: 2D charge versus $\Delta$t histogram segmented into 5 regions. The afterpulsing from Region 2 is referred to as 'Short' afterpulsing, Region 3 as 'Med' afterpulsing and Region 4 as 'Long' afterpulsing.

Fig. 4.10 shows the charges from each region individually and overlaid. The overlay histograms demonstrate that the charge distributions in each region contain a prominent SPE peak at 10 pC. Region 1, 2 and 3 have a low-charge pedestal that has a physical origin because there are a number of low charge hits shown in the charge versus $\Delta$t histogram. The charge distributions in Region 1 are mostly SPE and there are a small fraction of hits up to 3 PE. Since this distribution of hits occur within 50 ns of the triggered pulse, it is necessary to check if they have a physical origin. Fig. 4.12 shows an example Zero Length Encoded (ZLE) pulse of a Region 1 hit, demonstrating that they have a physical origin and are not caused by the Pulsefinder. There is a distinct distribution of high charge hits in Region 2

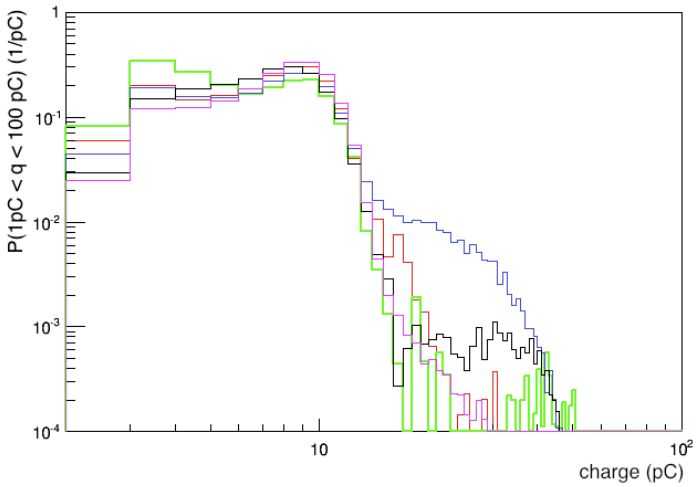


(a)

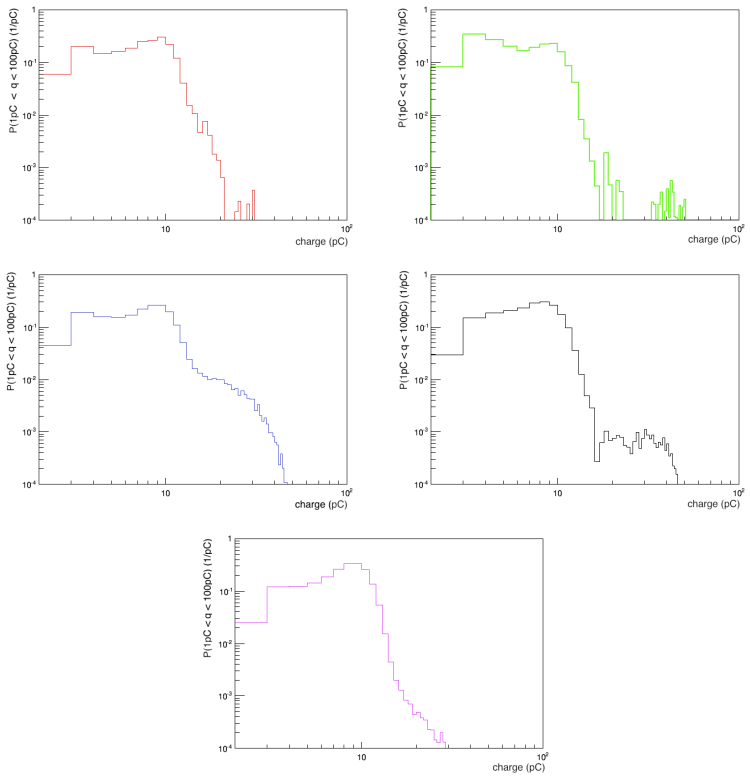

Figure 4.10: SubFig. 4.10a shows the overlay for each charge region with Region 1 (red), Region 2 (green), Region 3 (blue), Region 4 (black) and Region 5 (pink). The individual histograms for each region are also shown.

that also have a physical origin as shown in Fig. 4.12. Region 3 contains a prominent 2 PE and 3 PE high charge tail. Region 4 has a distinct collection of high charge hits between 2 PE to 4 PE. The multiple PE hits in the dark noise region are randomly distributed in $\Delta$t.

To understand the implications for event selection and filtering due to the above features, the charge versus $\Delta$t distribution for multiple PE hits is shown in Fig. 4.12 and Fig. **??**. It is important to identify methods of rejecting these pulses because they are potentially the source of anomalous physics triggers. The high charge hits in Region 1 occur between 35 ns to 100 ns. There are also two distinct peaks at 2 $\mu$s and 6 $\mu$s. The multiple PE pulses in Region 2 can possibly be identified because of their time correlation. The high charge pulses in Region 3, 4 and 5 may have to be rejected via pulse shape discrimination.

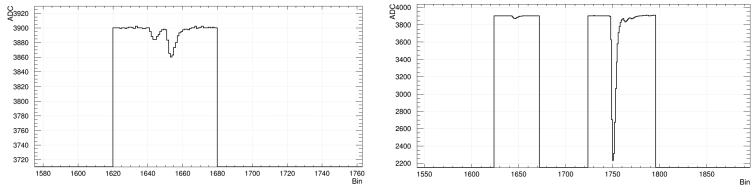


Figure 4.11: TOP LEFT: Example of a raw ZLE waveform of a hit in Region 1. TOP RIGHT: Example of a raw ZLE waveform of a hit in Region 2.

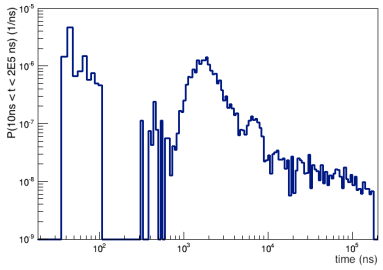


Figure 4.12: Charge versus $\Delta$t histogram for pulses in Region 2, 3 and 4 with charges greater than 1 PE.

# Chapter 5

# Dark noise and afterpulsing uniformity studies for all DEAP-3600 PMTs

## 5.1 Overview

Each PMT is not identical, meaning that the afterpulsing behavior and dark noise rate varies between each PMT. To understand this variation, a study of the detectors global afterpulsing and dark noise behavior is presented. The operating voltage, shown in Chapter 4, is a global setting that will be applied to all PMTs and can have a significant effect on the dark noise rate. It is therefore important to understand how it affects all the PMTs and is discussed in this chapter.

## 5.2 PMT uniformity

Using the method described in Chapter 3, the afterpulsing and dark noise uniformity for all PMTs can be checked. It would be incorrect to assume that all the PMTs are identical, so the

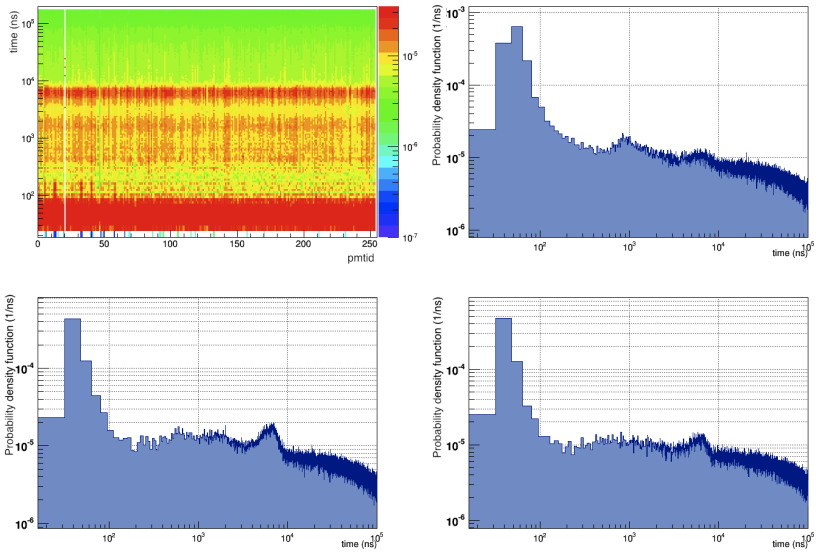


Figure 5.1: TOP LEFT: $\Delta$t vs PMT id plot for a dark run. The color axis represents the number of pulses in that particular bin. The blue stripe means that one PMT was not active during this run. The behavior for a typical PMT is shown in the BOTTOM LEFT figure. The TOP RIGHT and BOTTOM RIGHT figures show the $\delta$t distribution for PMT 128 and PMT 237 that have atypical late pulsing behavior. The dark blue color represents the 1D Y axis projection of the TOP LEFT figure. The light blue color is a color fill of the area below the data.

charge vs $\Delta t$ plots cannot be integrated over PMT id. The $\Delta t$ projection can be compared for each PMT as shown for a dark run in Fig. 5.1. A dark run was used for this study because each PMT is then subjected to the same conditions. There are several common features that are consistent for the vast majority of PMTs. Thus, each working PMT exhibits the sharp Coulomb backscattering peak between 70 ns to 90 ns. The afterpulsing between 400 ns to 3 $\mu$s exhibits a great degree of variation from PMT to PMT. PMT 237 is an example that exhibits a lower afterpulsing compared to other PMTs. The 1D time projection shows that there is pulsing in this region, however the number of pulses aren't vastly greater than the expected number of dark noise pulses. With the exception of PMT 237, each PMT exhibits a secondary distinct afterpulse between 7 $\mu$s to 9 $\mu$s.

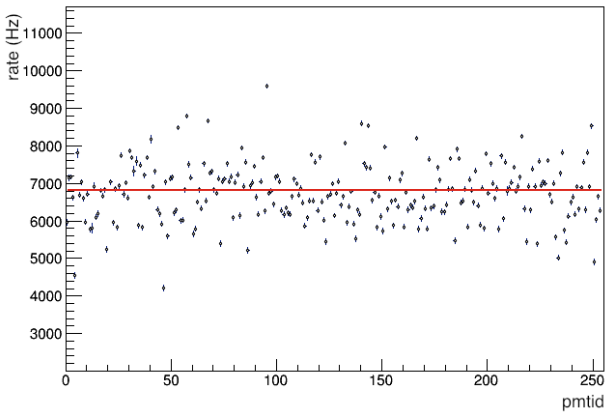
rate (Hz)
11000
10000
9000
8000
7000
6000
5000
4000
3000
0
50
100
150
200
250
pmtid

(a)

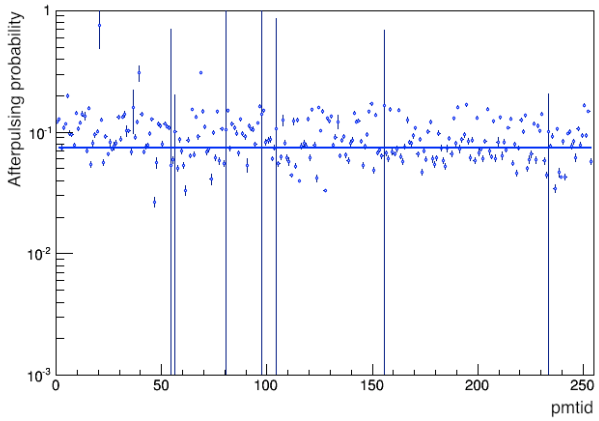
Afterpulsing probability
1
$10^{-1}$
$10^{-2}$
$10^{-3}$
0
50
100
150
200
250
pmtid

(b)

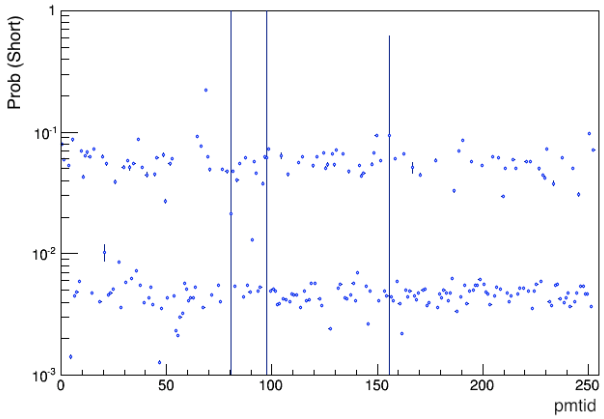
Prob (Short)
1
$10^{-1}$
$10^{-2}$
$10^{-3}$
0
50
100
150
200
250
pmtid

(c)

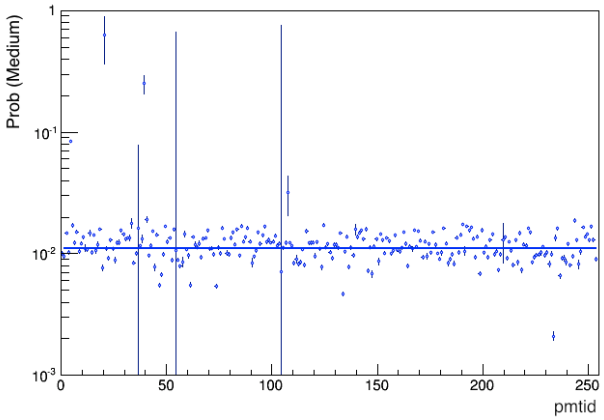


(d)

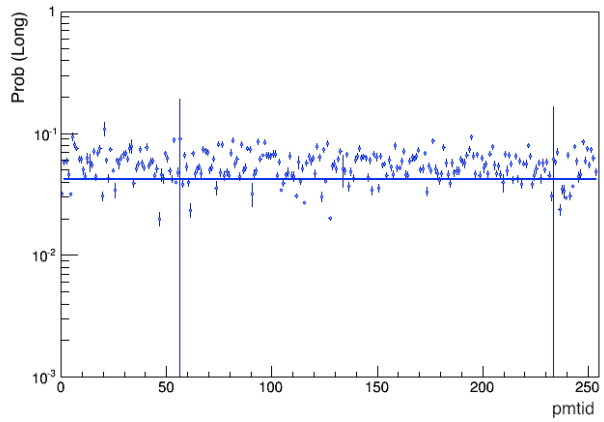


(e)

Figure 5.2: SubFig. 5.2a shows the dark noise fit output for all PMTs during a dark run. SubFig. 5.2b shows the total afterpulsing fit output for all PMTs. SubFig. 5.2c shows the short window (region 2) afterpulsing fit output for all PMTs. SubFig. 5.2d shows the medium window (region 3) afterpulsing fit output for all PMTs. SubFig. 5.2e shows the long window (region 4) afterpulsing fit output for all PMTs.

The global behavior of the fit parameters for all PMTs are shown in Fig. 5.2. The mean dark noise rate is 6823 Hz ± 4 Hz. There are no PMTs that have a fit dark noise rate above 12 kHz, which is the upper limit of the measured Hamamatsu value [59]. The fitted afterpulsing probabilities have a greater degree of variation where the total mean is 9.62% ± 0.87% . This is based on the sum of afterpulsing probabilities between 200 ns to 750 ns

(Short window), 750 ns to 5 $\mu$s (Medium window) and 5 $\mu$s to 10 $\mu$s (Long window). There are two distinct behaviors where approximately half of the PMTs have a short window afterpulsing probability of 5% and the other half have a probability of 0.5%. The mean medium window afterpulsing probability is 1.11% $\pm$ 0.02%. The long window probability is found to be 7.36% $\pm$ 0.18%.

## 5.3 Global AARF vs dark run study

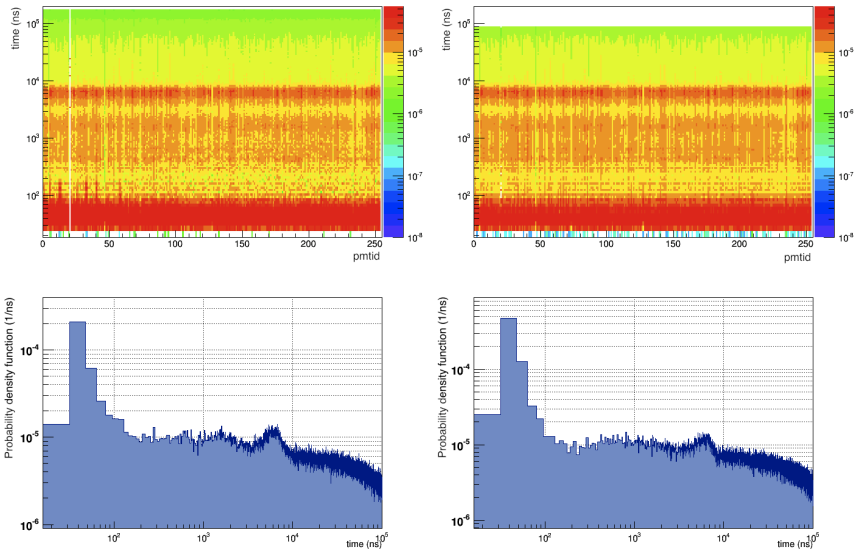


Figure 5.3: The color axis represents the number of pulses in that particular bin. TOP LEFT: $\Delta$t vs PMT id plot for an AARF run. There are several vertical red stripes which are the distributions for the PMTs that receive the most AARF light. TOP RIGHT: $\Delta$t vs PMT id plot for an AARF run. BOTTOM LEFT and BOTTOM RIGHT: $\Delta$t distributions for PMT 234 and 237, respectively, which seem to exhibit slightly different late pulsing spectra compared to other PMTs. The dark blue color represents the 1D Y axis projection of the top figures. The light blue color is a color fill of the area below the data.

The global behavior for afterpulsing induced from an AARF and dark run was also investigated, as shown in Fig. 5.3. Both run types exhibit similar characteristics for the groups of afterpulses between 70 ns to 90 ns, 400 ns to 3 $\mu$s and 7 $\mu$s to 9 $\mu$s. However there appears to be a slight variation in the number of pulses between 90 ns to 400 ns and between 3 $\mu$s

to 7 $\mu$s. There are also a set of PMTs between PMT 230 to 240 that show lower numbers of late pulses compared to other PMTs. The $\Delta$t spectrum for two of these PMTs are shown in Fig. 5.3. They still retain the same major afterpulsing features as the other PMTs albeit with lower incidences.

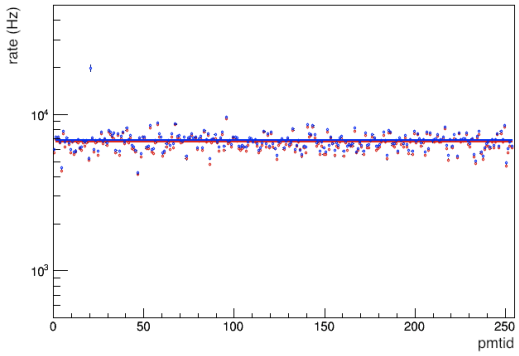


(a)

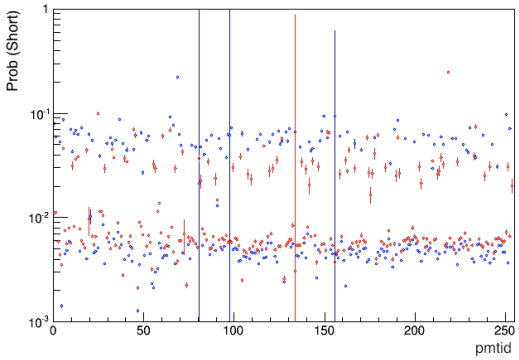


(b)

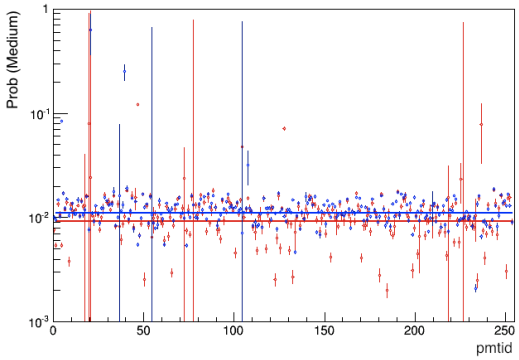


(c)

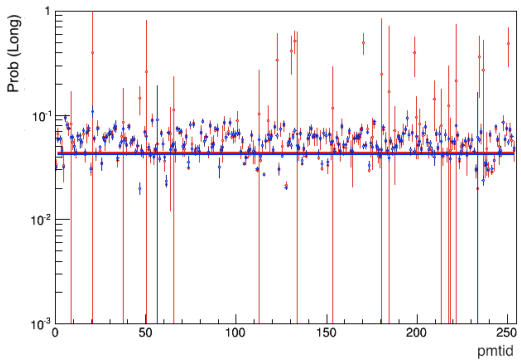


(d)

Figure 5.4: SubFig. 5.4a shows the overlay for the dark rate fit parameters of dark (blue) and AARF (red) runs for all PMTs. SubFig. 5.4b shows the overlay for the short window afterpulse fit parameters of dark (blue) and AARF (red) runs for all PMTs. SubFig. 5.4c shows the overlay for the medium window afterpulse fit parameters of dark (blue) and AARF (red) runs for all PMTs. SubFig. 5.4d shows the overlay for the long window afterpulse fit parameters of dark (blue) and AARF (red) runs for all PMTs.

Fig. 5.4 shows an overlay of the fit output for the AARF and dark runs. The mean AARF dark noise rate is 6823 Hz ± 4 Hz and the mean dark noise rate for the dark run is 6631 Hz ± 4 Hz. These agree within $1\sigma$ but the fit precision may be improved using increased statistics in future studies. For the short window afterpulsing, the fit probability is an order of magnitude larger for approximately half of all PMTs. The mean medium afterpulsing probability for the AARF and dark dataset are 0.90 % ± 0.04 % and 1.10 % ± 0.02 %, respectively. The mean long afterpulsing probability for the AARF and dark dataset are 4.33 % ± 0.21 % and 4.22 % ± 0.14 %. The mean total afterpulsing probability for the AARF and dark dataset are 6.82 % ± 0.28 % and 7.36 % ± 0.18 %.

## 5.4 Charge Uniformity for all PMTs

Using the same method as described in the previous chapter the charge distributions for all PMTs are plotted in Fig. 5.5. For each charge region there is a distinct SPE peak for all PMTs. There also is a distinct sub SPE peak in Regions 1, 2 and 3. Regions 1 and 3 have a multiple PE tail and Regions 2 and 4 have a distinct multiple PE band of hits. Region

3 has possible dark noise hits subtracted from it and there is a random distribution of hits between the SPE band and multiple PE band in Regions 2 and 4. This implies that there are likely to be randomly distributed afterpulses between the two bands.

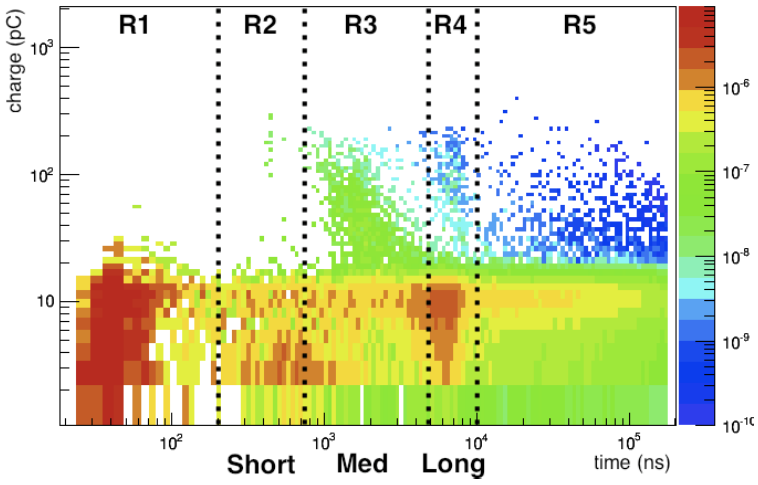


(a)

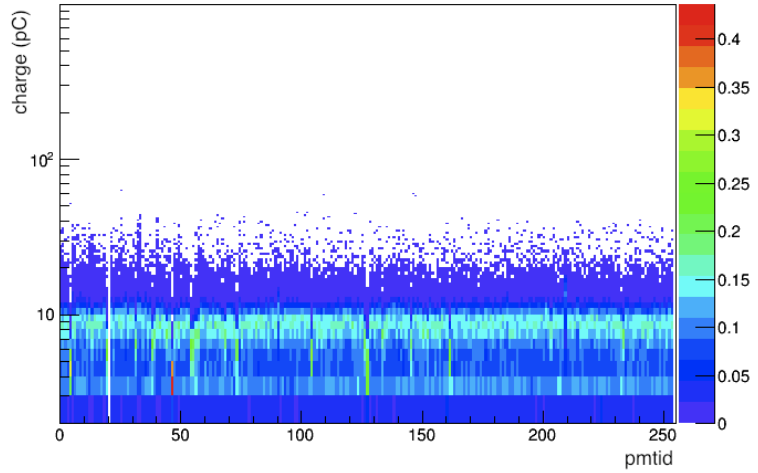


(b)

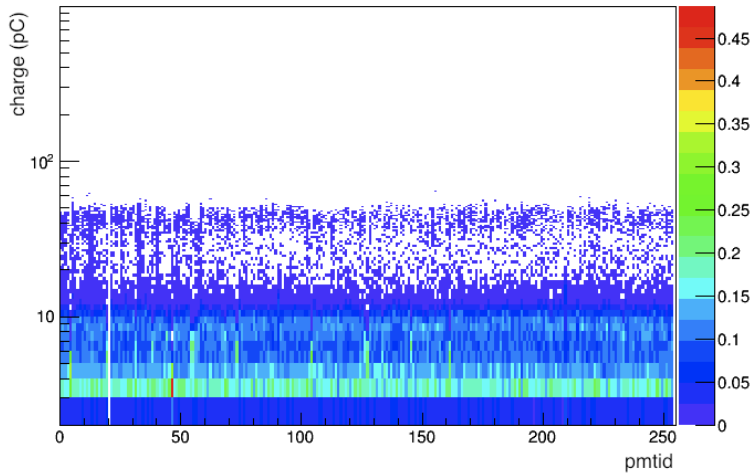
charge (pC)
$10^2$
10
0
50
100
150
200
250
pmtid
0.45
0.4
0.35
0.3
0.25
0.2
0.15
0.1
0.05
0

(c)

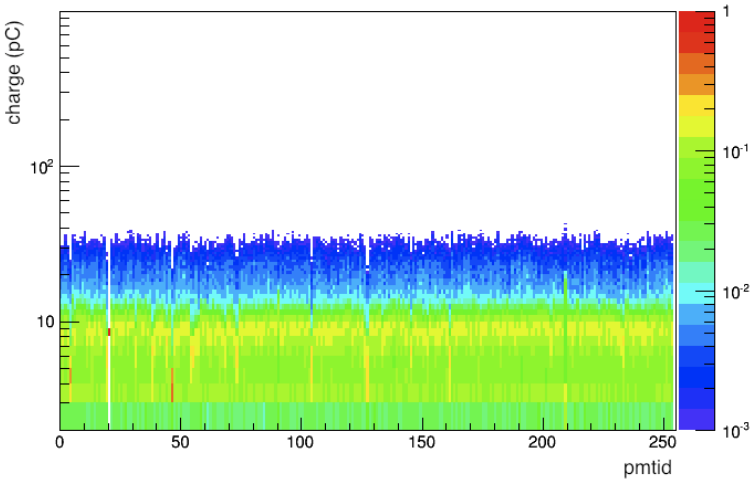
charge (pC)
$10^2$
10
0
50
100
150
200
250
pmtid
1
$10^{-1}$
$10^{-2}$
$10^{-3}$

(d)

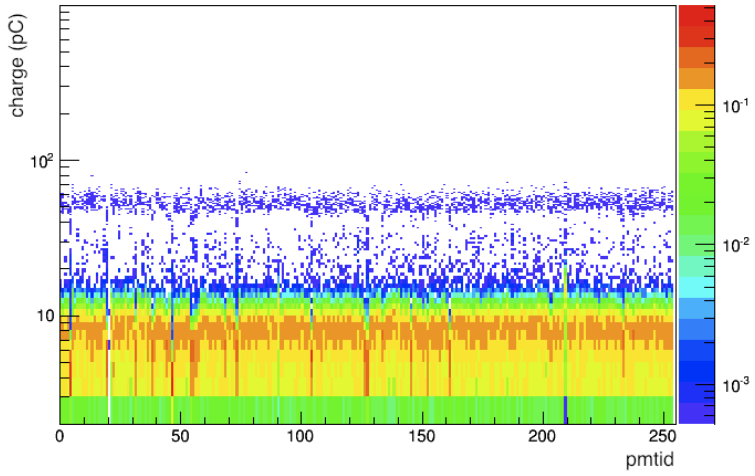


(e)

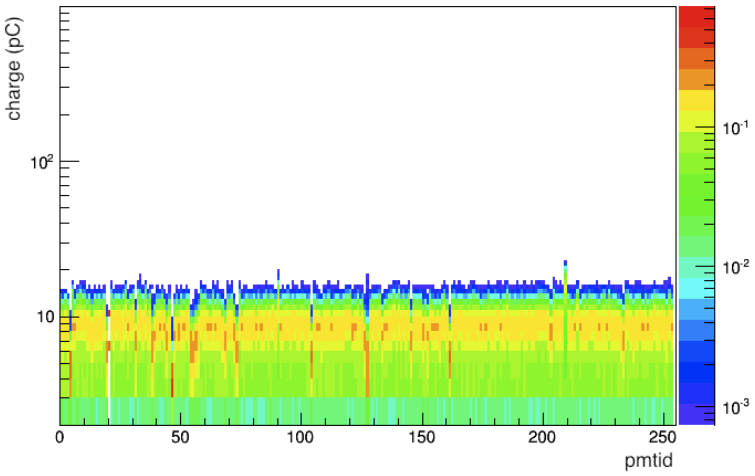


(f)

Figure 5.5: The color axis represents the number of pulses in that particular bin. SubFig. 5.5a shows the charge segmented regions. SubFig. 5.5b shows the charge distribution in Region 1 for all PMTs. SubFig. 5.5c shows the charge distribution in Region 2 for all PMTs. SubFig. 5.5d shows the charge distribution in Region 3 for all PMTs. SubFig. 5.5e shows the charge distribution in Region 4 for all PMTs. SubFig. 5.5f shows the charge distribution in Region 5 for all PMTs.

## 5.5 Voltage scan study of PMT uniformity

As discussed in Chapter 3, another factor that can affect the dark noise rates and afterpulsing for all PMTs is the operating voltage for each PMT. Fig. 5.6 shows the fit results for all PMTs taken between 50 V above the nominal voltage and 150 V below the nominal voltage. The dark noise rate is not expected to have a significant variation in this range so this study provides an indication of the ideal operating voltage for DEAP-3600. The fit of the mean dark noise rate is given by

$$\text{DNR} = 0.85(\text{Hz/V})V_0 + 6580.92 \text{ Hz}, \tag{5.1}$$

where DNR is the dark noise rate and $V_0$ is applied voltage. There is an increase in the mean dark noise rates by a factor of 2.57 as a function of voltage. The short afterpulsing behavior seems to be non linear and the short afterpulsing probability decreases by a factor of 3 between -150 V to -100 V. Between -100 V to +50 V the mean short window afterpulsing probability increases linearly and the fit is given by

$$PAP_{\text{short}} = 3.38 \times 10^{-5}(\text{Hz/V})V_0 + 0.59\%. \tag{5.2}$$

Between these two voltage ranges there is a factor of 1.42 increase in mean afterpulsing probability. The variation of the mean short window afterpulsing is less significant over this voltage range and the linear fits are given by

$$\begin{aligned} PAP_{\text{medium}} &= 6.07 \times 10^{-6}(\text{Hz/V})\ V_0 + 1.07\% \\ PAP_{\text{long}} &= 5.17 \times 10^{-6}(\text{Hz/V})\ V_0 + 5.15\%, \end{aligned} \tag{5.3}$$

where $PAP_{\text{medium}}$ and $PAP_{\text{long}}$ are the mean medium and long window afterpulsing probabilities. The mean medium and long afterpulsing probabilities increase by a factor of 0.12 and 0.11, respectively.

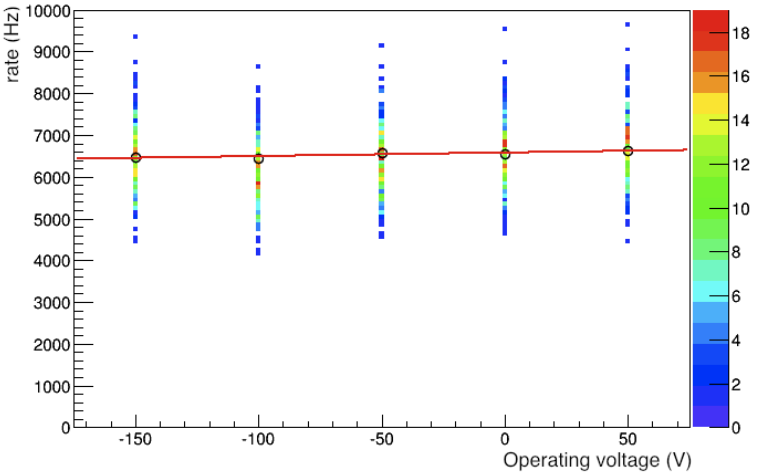
rate (Hz)
10000
9000
8000
7000
6000
5000
4000
3000
2000
1000
0
-150
-100
-50
0
50
Operating voltage (V)
18
16
14
12
10
8
6
4
2
0

(a)

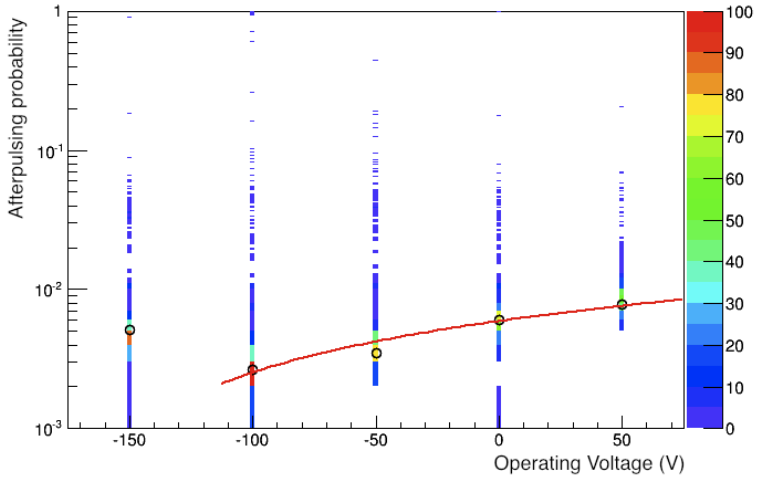
Afterpulsing probability
1
$10^{-1}$
$10^{-2}$
$10^{-3}$
-150
-100
-50
0
50
Operating Voltage (V)
100
90
80
70
60
50
40
30
20
10
0

(b)

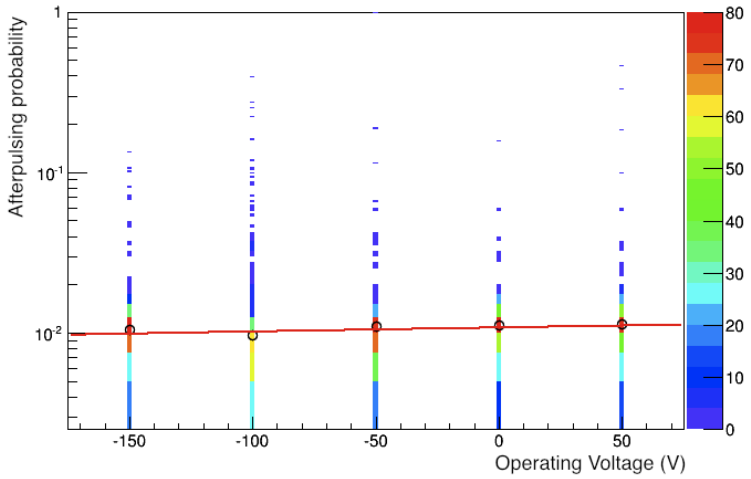


(c)

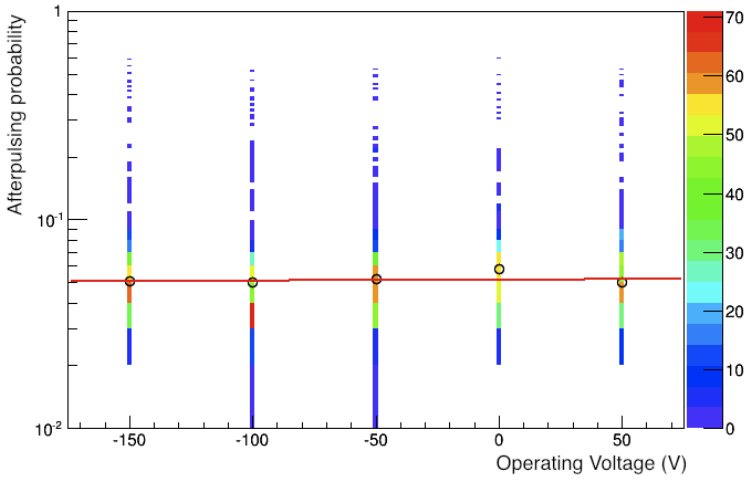


(d)

Figure 5.6: SubFig. 5.6a shows the fitted dark noise rate for all PMTs at different operating voltages. SubFig. 5.6b shows the fitted short window afterpulsing probability for all PMTs at different operating voltages. SubFig. 5.6c shows the fitted medium window afterpulsing probability for all PMTs at different operating voltages. SubFig. 5.6d shows the fitted long window afterpulsing probability for all PMTs at different operating voltages.

# Chapter 6

# Conclusion

We have discussed a methodology that can be used to characterize the extent of dark noise and afterpulsing in the DEAP-3600 detector. By counting the charge and time distributions of the triggered and first late pulse, an analytic PDF can be built for each PMT. Using this PDF we can potentially improve the discrimination efforts remove afterpulse induced triggers and set a low energy threshold to filter out dark noise events at the Eventbuilder level.

Through the preliminary studies presented here, we have shown that there are a number of distinct late pulsing behaviors that all the PMTs exhibit, including that 10 $\mu$s after the triggered pulse there are only dark noise pulses remaining. There are 4 fitted main afterpulses at about 70 ns, 0.7 ns to 0.75 $\mu$s, 0.75 $\mu$s to 3 $\mu$s and between 3 $\mu$s to 7 $\mu$s. The afterpulses at 70 ns and between 3 $\mu$s to 7 $\mu$s appear very consistently from PMT to PMT. The afterpulses 0.7 $\mu$s to 3 $\mu$s exhibit transitory behavior and a shape that varies from PMT to PMT. By comparing AARF run data to dark run data, it is found the afterpulsing from an external single photoelectron produces the same afterpulsing behavior as a dark noise photon. By applying the presented fit method we were able to show that the dark rates of the PMTs peak around 6 kHz at nominal voltage and the total afterpulsing probability is between 1 % to 4 %. We were able to show that changing the operating voltage from -150 V to 50 V around the nominal value did not significantly change the dark noise rates, but did cause a slight increase in the afterpulsing probabilities.

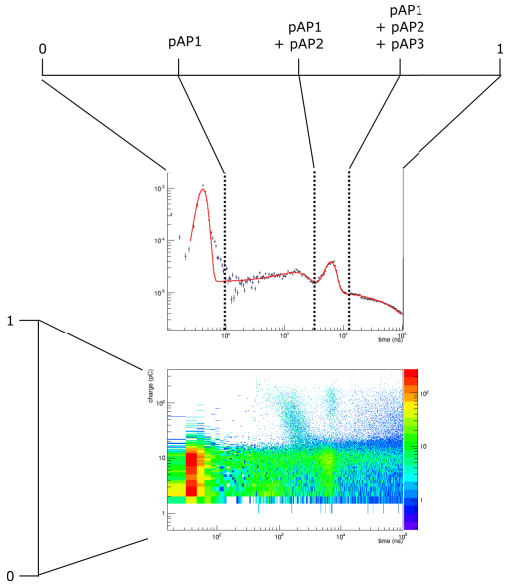


Figure 6.1: Example workflow of how the RAT simulation could be implemented using the fitted $\Delta$t and charge versus $\Delta$t distribution for each PMT.

## 6.1 Applications in the simulation workflow

This afterpulsing analysis can be implemented into the DEAP collaboration's RAT simulation. This would enable the low energy threshold contribution from dark noise to be defined. Additionally, afterpulsing simulations would help mitigate the chances of triggering on afterpulses. The implementation in the simulation workflow would involve generating a PDF using the fit parameters. Two objects for each PMT would be written in the simulation workflow, a charge versus $\Delta$t plot and a fitted $\Delta$t 1D projection. For each simulated triggered pulse a random number could then determine which afterpulsing time to generate. By generating another random number, the charge can be simulated using the tabulated charge versus $\Delta$t plot, and using the $\Delta$t projection the number of late pulses can be simulated.

## 6.2 Effects on Fprompt and trigger settings

There are a number of ways the trigger level filter and Fprompt filtering can be used to mitigate the effects of afterpulsing and dark noise. There are two stages in which the late

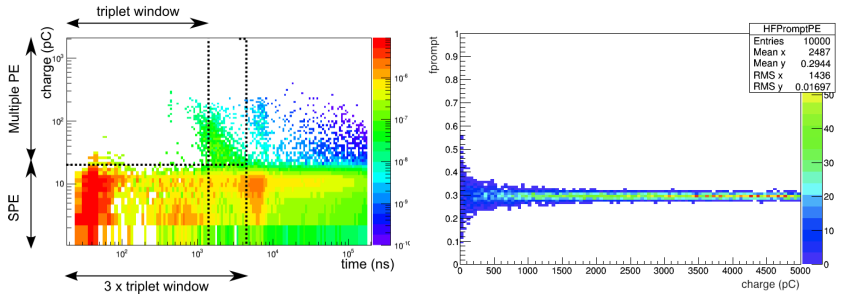


Figure 6.2: Example workflow of how the RAT simulation could be implemented using the fitted $\Delta$t and charge versus $\Delta$t distribution for each PMT.

pulse triggering can lead to an anomalous dark matter signal, if an afterpulsing is triggered and passes the Eventbuilder level of the experiment. As shown in Fig. 6.2, pulses after 1.5 $\mu$s will not be used in the calculation of Fprompt. This should mitigate the effects of the dominant source of afterpulsing and dark noise affecting the Fprompt calculation. This still leaves a number of afterpulses that can be incorrectly triggered on. The multiple PE hits can be mitigated by setting the Event Builder filter to exclude hits greater than 1 PE and less than 50 PE that occur between 100 ns to 1.5 $\mu$s after the triggered pulse. This reduces the afterpulsing triggering to a level of about 2%.

This leaves two sources of SPE afterpulsing triggers: the Coulomb backscattering hits between 30 ns to 100 ns and a potential ion induced afterpulse between 400 ns to 1.2 $\mu$s. These afterpulsing hits can be mitigated by evaluating the Fprompt versus energy parameter as shown in Fig. 6.2 which shows a Fprompt-Energy plot produced from a Monte Carlo simulation of hits induced from afterpulsing and dark noise sources. Therefore, based on this distribution it seems that the remaining two afterpulsing sources can be mitigated at the Event Builder filter because they do not have Fprompt values large enough to occur in the WIMP region of interest.

# Bibliography


[1] F. Zwicky, "On the Masses of Nebulae and of Clusters of Nebulae," *The Astrophysical Journal*, vol. 86, p. 217, Oct. 1937. [Online]. Available: http://adsabs.harvard.edu/abs/1937ApJ....86..217Z

[2] Planck Collaboration, "Planck 2015 results. XIII. Cosmological parameters," *arXiv:1502.01589 [astro-ph]*, Feb. 2015, arXiv: 1502.01589. [Online]. Available: http://arxiv.org/abs/1502.01589

[3] A. Kusenko and L. J. Rosenberg, "SNOWMASS-2013 Cosmic Frontier 3 (CF3) Working Group Summary: Non-WIMP dark matter," *arXiv*, Oct. 2013. [Online]. Available: http://arxiv.org/abs/1310.8642

[4] S. P. Martin, "A Supersymmetry Primer," *Adv.Ser.Direct.High Energy Phys.*, vol. 21, pp. 1–153, Sep. 2012. [Online]. Available: http://arxiv.org/abs/hep-ph/9709356

[5] DEAP-3600 collaboration, "DEAP-3600 Dark Matter Search," *arXiv:1410.7673 [astro-ph, physics:hep-ex, physics:physics]*, Oct. 2014, arXiv: 1410.7673. [Online]. Available: http://arxiv.org/abs/1410.7673

[6] V. C. Rubin *et. al*, "Motion of the Galaxy and the local group determined from the velocity anisotropy of distant SC I galaxies. I - The data," *The Astronomical Journal*, vol. 81, pp. 687–718, Sep. 1976. [Online]. Available: http://adsabs.harvard.edu/abs/1976AJ.....81..687R

[7] P. Peebles, "Large scale background temperature and mass fluctuations due to scale invariant primeval perturbations," *Astrophysics Journal*, vol. 263, 1982.

[8] G. R. Blumenthal *et. al*, "Formation of galaxies and large-scale structure with cold dark matter," *Nature*, vol. 311, pp. 517 – 525, 1984.

[9] J. R. Bond, A. S. Szalay, and M. S. Turner, "Formation of galaxies in a gravitino-dominated universe," *Phys. Rev. Lett.*, vol. 48, no. 1636, 1982.

[10] H. Baer, "Supersymmetry and Dark Matter post LHC8: why we may expect both axion and WIMP detection," *arXiv*, pp. 289–296, 2014. [Online]. Available: http://arxiv.org/abs/1310.1859

[11] G. Bertone, D. Hooper, and J. Silk, "Particle Dark Matter: Evidence, Candidates and Constraints," *Physics Reports*, vol. 405, no. 5-6, pp. 279–390, Jan. 2005.

[12] B. Carroll and D. Ostlie, "An Introducton to Modern Astrophysics," Pearson Ed., 2007.

[13] M. Drees and G. Gerbier, "Mini–Review of Dark Matter: 2012," *arXiv*, Apr. 2012, https://inspirehep.net/record/1108152?ln=en. [Online]. Available: http://arxiv.org/abs/1204.2373

[14] M. Kamionkowski, "WIMP and Axion Dark Matter," *Trieste 1997, High energy physics and cosmology*, pp. 394–411, Oct. 1997. [Online]. Available: http://arxiv.org/abs/hep-ph/9710467

[15] J. Bovy and S. Tremaine, "On the Local Dark Matter Density," *The Astrophysical Journal*, vol. 756, no. 1, 2012.

[16] K. Freese, "Review of observational evidence for dark matter in the universe and in upcoming searches for dark stars," *European Astronomical Society*, vol. 36, pp. 113–126, Dec 2009. [Online]. Available: http://arxiv.org/pdf/0812.4005.pdf

[17] R. A. Cabanac *et. al*, "Discovery of a high-redshift Einstein ring," *Astronomy and Astrophysics*, vol. 436, no. 2, pp. L21–L25, Jun. 2005. [Online]. Available: http://arxiv.org/abs/astro-ph/0504585

[18] C. S. Kochanek, C. R. Keeton, and B. A. McLeod, "The Importance of Einstein Rings," *The Astrophysical Journal*, vol. 547, no. 1, pp. 50–59, Jan. 2001. [Online]. Available: http://arxiv.org/abs/astro-ph/0006116

[19] K. Griest, "The Search for Dark Matter: WIMPs and MACHOs," *Annals of the New York Academy of Sciences*, vol. 668, no. 1, March 1993.

[20] R. Massey, T. Kitching, and J. Richard, "The Dark Matter of Gravitational Lensing," *Reports on Progress in Physics*, vol. 73, no. 8, Aug. 2010. [Online]. Available: http://arxiv.org/abs/1001.1739

[21] EROS2 collaboration, "Limits on the MACHO Content of the Galactic Halo from the EROS-2 Survey of the Magellanic Clouds," *Astronomy and Astrophysics*, vol. 469, no. 2, pp. 387–404, Jul. 2007. [Online]. Available: http://arxiv.org/abs/astro-ph/0607207

[22] T. Lasserre, "EROS2 microlensing search towards the Magellanic Clouds," in *ASP Conference Proceedings*, T. G., Ed., vol. 237, Sep. 1999, p. 239. [Online]. Available: http://adsabs.harvard.edu/full/2001ASPC..237..239L

[23] M. Markevitch, "Intergalactic shock fronts," in *12th Marcel Grossmann Meeting on General Relativity*, T. Damour, Ed., 2009, pp. 397–410. [Online]. Available: http://arxiv.org/pdf/1010.3660.pdf

[24] R. Thompson, R. Davé, and K. Nagamine, "The rise and fall of a challenger: the Bullet Cluster in lambda Cold Dark Matter simulations," *Monthly Notices of the Royal Astronomical Society*, vol. 452, no. 3, Oct. 2014.

[25] S. Weinberg, "Cosmology," Oxford University Press, 2008.

[26] WMAP collaboration, "Nine-Year Wilkinson Microwave Anisotropy Probe (WMAP) Observations: Cosmological Parameter Results," *The Astrophysical Journal Supplement Series*, vol. 208, no. 2, p. 19, Oct. 2013. [Online]. Available: http://arxiv.org/abs/1212.5226

[27] V. Springel *et. al*, "Simulating the joint evolution of quasars, galaxies and their large-scale distribution," *Nature*, vol. 435, no. 7042, pp. 629–636, Jun. 2005. [Online]. Available: http://arxiv.org/abs/astro-ph/0504097

[28] S. Profumo, "TASI 2012 Lectures on Astrophysical Probes of Dark Matter," *arXiv*, Jan. 2013. [Online]. Available: http://arxiv.org/abs/1301.0952

[29] D. N. Schramm, "The Big Bang and Other Explosions in Nuclear and Particle Astrophysics," World Scientific, 1996.

[30] W. J. Percival *et. al*, "The 2df galaxy redshift survey: the power spectrum and the matter content of the universe," *Monthly Notices of the Royal Astronomical Society*, vol. 327, no. 4, pp. 1297–1306, 2001.

[31] X. X. Xue *et. al*, "The Milky Way's Circular Velocity Curve to 60 kpc and an Estimate of the Dark Matter Halo Mass from the Kinematics of $\sim$ 2400 SDSS Blue Horizontal-Branch Stars," *The American Astronomical Society*, vol. 684, no. 2, 2008.

[32] NASA, ESA, and R. Massey, "Hubble Maps the Cosmic Web of "Clumpy" Dark Matter in 3-D," Jan 2007, COSMOS Field illustation. [Online]. Available: http://hubblesite.org/newscenter/archive/releases/2007/01/image/e/⟩

[33] ATLAS and CMS Collaborations, "Combined Measurement of the Higgs Boson Mass in pp Collisions at sqrt(s)=7 and 8 TeV with the ATLAS and CMS Experiments," *Physical Review Letters*, vol. 114, no. 19, May 2015, arXiv: 1503.07589. [Online]. Available: http://arxiv.org/abs/1503.07589

[34] M. Holthausen, K. S. Lim, and M. Lindner, "Planck scale boundary conditions and the Higgs mass," *Journal of High Energy Physics*, vol. 2012, no. 37, 2012.

[35] T. Cohen, D. J. Phalen, and A. Pierce, "On the Correlation Between the Spin-Independent and Spin-Dependent Direct Detection of Dark Matter," *Physical Review D*, vol. 81, no. 11, Jun. 2010, arXiv: 1001.3408. [Online]. Available: http://arxiv.org/abs/1001.3408

[36] J. L. Feng *et. al*, "Planning the Future of U.S. Particle Physics (SNOWMASS 2013): Chapter 4: Cosmic Frontier," in *Snowmass 2013*, 2013.

[37] SuperCDMS collaboration, "Search for Low-Mass WIMPs with SuperCDMS," *Physical Review Letters*, vol. 112, no. 24, Jun. 2014. [Online]. Available: http://arxiv.org/abs/1402.7137

[38] A. Zani, "The WArP Experiment: A Double-Phase Argon Detector for Dark Matter Searches," *Advances in High Energy Physics*, vol. 2014, 2014. [Online]. Available: http://www.hindawi.com/journals/ahep/2014/205107/fig1

[39] LUX Collaboration, "First results from the LUX dark matter experiment at the Sanford Underground Research Facility," *Physical Review Letters*, vol. 112, no. 9, Mar. 2014. [Online]. Available: http://arxiv.org/abs/1310.8214

[40] IceCube collaboration, "Search for Dark Matter Annihilations in the Sun with the 79-String IceCube Detector," *Phys. Rev. Lett.*, vol. 110, 2013. [Online]. Available: http://journals.aps.org/prl/pdf/10.1103/PhysRevLett.110.131302

[41] D. Bauer and J. Buckley *et. al*, "Dark Matter in the Coming Decade: Complementary Paths to Discovery and Beyond," *Physics of the Dark Universe*, vol. 7-8, pp. 16–23, Mar. 2015. [Online]. Available: http://arxiv.org/abs/1305.1605

[42] AMS collaboration, "First Result from the Alpha Magnetic Spectrometer on the International Space Station: Precision Measurement of the Positron Fraction in Primary Cosmic Rays of 350 GeV," *Phys. Rev. Lett.*, vol. 110, no. 14, Apr. 2013. [Online]. Available: http://link.aps.org/doi/10.1103/PhysRevLett.110.141102

[43] K. A. Olive and the Particle Data Group, "Review of Particle Physics," *Chinese Phys. C*, vol. 38, no. 9, p. 090001, Aug. 2014. [Online]. Available: http://iopscience.iop.org/1674-1137/38/9/090001

[44] S. Fukuda *et. al*, "The Super-Kamiokande detector," *Nuclear Instruments and Methods in Physics Research*, vol. A501, no. 2-3, pp. 418–462, April 2003.

[45] The ATLAS Collaboration, "Search for dark matter candidates and large extra dimensions in events with a jet and missing transverse momentum with the ATLAS detector," *Journal of High Energy Physics*, vol. 2013, no. 4, Apr. 2013. [Online]. Available: http://arxiv.org/abs/1210.4491

[46] T. Pollmann, "Alpha backgrounds in the DEAP Dark Matter search experiment," Ph.D. dissertation, Queen's University, 2012. [Online]. Available: http://deap3600.ca/Contents/thesis/PollmannTinaPhD.pdf

[47] C. Nantais, "Radiopurity measurement of acrylic for the DEAP-3600 dark matter experiment," Ph.D. dissertation, Queen's University, 2014. [Online]. Available: http://qspace.library.queensu.ca/handle/1974/8554

[48] B. Beltran *et. al*, "Background events from the DEAP-3600 neck components and TPB: a short note," University of Alberta, Tech. Rep., Dec. 2014.

[49] T. K. Gaisser, "Cosmic rays and particle physics," Cambridge University Press, 1990.

[50] T. Pollmann, "Alpha backgrounds in the DEAP dark matter search experiment." Ph.D. dissertation, Queen's University, 2012. [Online]. Available: http://qspace.library.queensu.ca/handle/1974/7362

[51] DEAP-I collaboration, "Measurement of the scintillation time spectra and pulse-shape discrimination of low-energy beta and nuclear recoils in liquid argon with DEAP-1," *arXiv*, Apr. 2009. [Online]. Available: http://arxiv.org/abs/0904.2930

[52] J. Xu *et. al*, "A Study of the Residual 39Ar Content in Argon from Underground Sources," *arXiv*, Apr. 2012. [Online]. Available: http://arxiv.org/abs/1204.6011

[53] V. V. Golovko *et. al*, "Muon Veto Detector for DEAP-3600 Dark Matter Experiment (64 PMTs)," TRIUMF, Tech. Rep., Mar. 2011.

[54] R. T. Chouinard, "Performance evaulation of signal conditioning boards and simulation of the impact of electronics noise on the DEAP-3600 dark matter

detector," Thesis, University of Alberta, Jan. 2013. [Online]. Available: http://hdl.handle.net/10402/era.30016,uuid:31bdf5af-05a2-480b-aa93-a60dd9eddf63

[55] F. Retiere, "DEAP-3600 Electronics & DAQ Technical Design Report," TRIUMF, Tech. Rep., Apr. 2011.

[56] T. Sonley, "DEAP 3600 PMT Selection," SNOlab, Tech. Rep., Oct. 2010.

[57] D. N. McKinsey and J. M. Doyle, "Liquid Helium and Liquid Neon - Sensitive, Low Background Scintillation Media For the Detection of Low Energy Neutrinos," *Journal of Low Temperature Physics*, vol. 118, no. 3-4, pp. 153–165, Jul. 1999. [Online]. Available: http://link.springer.com/article/10.1023%2FA%3A1004690906370

[58] Hamamatsu, "Photomultipler Tubes; Basics and Applications," Hamamatsu Photonics K.K, 2007.

[59] Hamamatsu Photonics K.K, "Large Photocathode Area Photomultiplier Tubes," Hamamatsu Photonics, Tech. Rep., 2008.

[60] R. L. Bell, "Negative electron affinity devices," Oxford University Press, Oxford, Aug. 1973.

[61] Philips Photonics, "Photomultipler tubes, principles and applications," Philips, 1994.

[62] P. Pasuthip, "Cold PMT test," Queen's University, Tech. Rep., Feb. 2014.

[63] J. Haser *et. al*, "Afterpulse measurements of R7081 photomultipliers for the Double Chooz experiment," *J. Inst.*, vol. 8, no. 04, Apr. 2013. [Online]. Available: http://iopscience.iop.org/1748-0221/8/04/P04029

[64] K. J. Ma *et. al*, "Time and Amplitude of Afterpulse Measured with a Large Size Photomultiplier Tube," *Nuclear Instruments and Methods in Physics Research Section A: Accelerators, Spectrometers, Detectors and Associated Equipment*, vol. 629, no. 1, pp. 93–100, Feb. 2011, arXiv: 0911.5336. [Online]. Available: http://arxiv.org/abs/0911.5336

[65] T. Li and T. Pollmann, "SPE Fitting," Mar. 2015, internal DEAP-3600 document.

[66] T. McElroy, "DSPE Pulse Finding and SPE counting in DEAP-3600," Mar. 2015, internal DEAP-3600 document.